Ore Geology Reviews 152 (2023) 105244

Contents lists available at ScienceDirect

Ore Geology Reviews

journal homepage: www.elsevier.com/locate/oregeorev

Mapping hydrothermal and supergene alteration zones associated with carbonate-hosted Zn-Pb deposits by using PRISMA satellite imagery supported by field-based hyperspectral data, mineralogical and geochemical analysis

Rita Chirico [a], Nicola Mondillo [a,b,*], Carsten Laukamp [c], Angela Mormone [d], Diego Di Martire [a], Alessandro Novellino [e], Giuseppina Balassone [a,d]

[a] Dipartimento di Scienze della Terra, dell'Ambiente e delle Risorse, Università degli Studi di Napoli Federico II, Complesso Universitario di Monte S. Angelo, Via Cintia 26, Napoli 80126, Italy
[b] Natural History Museum, London SW7 5BD, the United Kingdom of Great Britain and Northern Ireland
[c] CSIRO Mineral Resources, Kensington, WA 6151, Australia
[d] INGV Osservatorio Vesuviano, Via Diocleziano 328, Napoli 80124, Italy
[e] British Geological Survey, Environmental Science Centre, Keyworth, Nottingham NG12 5GG, UK

ARTICLE INFO

Keywords:
Hyperspectral data
Remote sensing
PRISMA
Reflectance spectra
Mineral exploration
Carbonate-hosted Zn deposits

ABSTRACT

Delineating hydrothermal alteration and supergene caps is fundamental for mineral exploration of sulfide ores. The aim of this study is to apply a multi-scale workflow based on hyperspectral remote and proximal sensing data in order to delineate hydrothermal dolomitization and supergene alteration associated with the Mississippi Valley-Type Zn-Pb(-Ag) deposit of Jabali (Western Yemen). The area was investigated through hyperspectral images derived from the new launched Italian Space Agency's PRISMA satellite, which has a higher spectral resolution compared to multispectral sensors and covers the mineral-diagnostic wavelength regions (such as the 2100 nm to 2300 nm range) with a Signal to Noise Ratio (SNR) $\geq$ 100. Spectral mineral maps were produced through the band ratios method using specific feature extraction indices applied to the hyperspectral satellite data. The results were validated by using Visible Near InfraRed (VNIR) to Short Wave InfraRed (SWIR) reflectance spectra, mineralogical (XRPD) and geochemical (ICP-ES/MS) analyses on rock samples collected in the Jabali area. The dolomites footprint was mapped using a PRISMA Level 2C image, by enhancing the spectral differences between limestones and dolomites in the SWIR-2 region (major features centered at 2340 nm and 2320 nm, respectively). Gossans were detected due to the Fe^{3+} absorption band in the VNIR region at 900 nm. The Zn-Pb mineralized area, extended for approximately 25 km^2, was thus identified by recognizing gossan occurrences in dolomites. The study demonstrates that the PRISMA satellite is effective in identifying Zn-Pb mineralized outcrops in sedimentary basins.

1. Introduction

Spectral remote sensing technology represents a tool that has been well-established in applied geology for over four decades (Bedini, 2017; Peyghambari and Zhang, 2021; and reference therein). The main aim of spectral remote sensing is to detect and quantitatively measure the earth's surface materials, by using calibrated reflectance spectra acquired as images in hundreds of narrow and contiguous spectral bands, generally ranging from the Visible Near InfraRed (VNIR; 400 to 1300 nm) to Short Wave InfraRed (SWIR; 1300 to 2600 nm) regions of the electromagnetic spectrum (Van der Meer et al., 2012). Several rock-forming and alteration minerals show diagnostic spectral absorptions in the VNIR, SWIR 1 (1300–1850 nm), and SWIR 2 (1850–2600 nm) wavelength ranges. These wavelength ranges are suitable for geological

* Corresponding author at: Dipartimento di Scienze della Terra, dell'Ambiente e delle Risorse, Università degli Studi di Napoli Federico II, Complesso Universitario di Monte S. Angelo, Via Cintia 26, Napoli 80126, Italy.
E-mail addresses: rita.chirico@unina.it (R. Chirico), nicola.mondillo@unina.it (N. Mondillo), carsten.laukamp@csiro.au (C. Laukamp), angela.mormone@ingv.it (A. Mormone), diego.dimartire@unina.it (D. Di Martire), alessn@bgs.ac.uk (A. Novellino), balasson@unina.it (G. Balassone).

https://doi.org/10.1016/j.oregeorev.2022.105244
Received 17 September 2022; Received in revised form 24 November 2022; Accepted 2 December 2022
Available online 6 December 2022

Table 1
Reference spectral reflectance features of the main host-rock and supergene alteration minerals observed in the Jabali samples.

Mineral	Formula	Characteristic spectral features in VNIR	Characteristic spectral features in SWIR	References
Dolomite	$CaMg(CO_3)_2$	Fe^{2+} broad double absorption band centered at 1200 nm (only for ferroan dolomites)	CO_3 at 2320 nm (major). Shifted to longer wavelengths for ferroan dolomites.	Gaffey (1986)
Calcite	$CaCO_3$	Fe^{2+} broad double absorption band centered at 1300 nm (only for ferroan calcites)	CO_3 at 1750 nm and 2160 nm (min); 2335 nm (major). Shifted to longer wavelengths for ferroan calcite.	Gaffey (1986)
Smithsonite	$ZnCO_3$	Red peak; broad depression at 800–1200 nm	CO_3 at 2320 nm (min) and 2360 nm (major)	McConachy et al. (2007)
Hydrozincite	$Zn_5(CO_3)_2(OH)_6$	Peak at 600 nm	OH at 1430 nm and 1500 nm; CO_3 at 2300 nm and 2390 nm (major); min unknown at 1800 nm, 1850 nm, 1970 nm and 2025 nm	McConachy et al. (2007)
Goethite	α-FeO(OH)	Peak at 764 nm; CTF at 480 nm and 670 nm (min), and CFA at 940 nm (major)	OH and H_2O at 1451 nm and 1935 nm	Crowley et al. (2003); Cudahy and Ramanaidou (1997)
Hematite	α-Fe_2O_3	Peak at 749 nm; CFA at 880 nm		Crowley et al. (2003); Cudahy and Ramanaidou (1997)
Hemimorphite	$Zn_4Si_2O_7(OH)_2H_2O$		OH and H_2O at 975 nm, 1160 nm, 1400 nm and 1940 nm; weak Zn–OH (?) at 2210 nm	McConachy et al. (2007)
Sauconite	$Na_{0,3}Zn_3(Si, Al)_4O_{10}(OH)_2(H_2O)$		H_2O at 1910 nm and OH at 1420 nm; possible Zn–OH at 2305 nm	McConachy et al. (2007)
Jarosite	$KFe_3(SO_4)_2(OH)_6$	Peak at 717 nm; CFT at 437 nm and CFA at 911 nm (major)	OH (and adsorbed H_2O) at 1467 nm, 1849 nm and 1936 nm; Fe-OH at 2264	Crowley et al. (2003); Cudahy and Ramanaidou (1997)

spectral sensing applications as they provide mineralogical and geochemical information due to electronic transitions and vibrational processes in minerals (Clark et al., 1990). Characteristic spectral features can be used for defining the occurrence and relative abundance of mineral species and their physicochemical variations (Laukamp et al., 2021). Since its advent, geological remote sensing has been used as a tool for the exploration of mineral deposits. Even though spectral sensing has been applied to the study and exploration of several ore deposit types through different scales of observation (e.g., Lampinen et al., 2017; Bedini 2017; Laukamp et al., 2022, and references therein), its potential still remains underexplored for the investigation of several ore minerals of notable economic importance. At the same time, more advanced satellites are launched ever more frequently, making the available spectral data increasingly detailed in both the spatial and the spectral resolution (i.e. hyperspectral systems are characterized by a higher number of channels compared to multispectral sensors; Peyghambari and Zhang, 2021). The present study aims to test the effectiveness of the newly launched Italian Space Agency's (ASI) PRISMA (Precursore IperSpettrale della Missione Applicativa) hyperspectral satellite for the exploration of carbonate-hosted base metal deposits. The application of hyperspectral remote sensing technology in the exploration of carbonate-hosted base-metal and Mississippi Valley-type (MVT) deposits is challenging for two main reasons: (1) the limited wavelength range needed for distinguishing the carbonate minerals and, (2) the limited availability of hyperspectral imagery covering longer wavelength regions where the carbonate minerals are active (Bedini 2017). Large scale features potentially allow the application of spectral remote sensing techniques to the exploration of carbonate-hosted ore deposits. They include, firstly, the hydrothermally derived dolomites, which in most cases are spatially and temporally associated with base-metal mineralization (Leach et al., 2005). Secondly, gossans, which are mostly composed of high amounts of Fe-oxides and hydroxides and associated with the supergene weathering of the buried sulfide orebodies (Taylor 2011). In this study, we propose a methodology based on remote and proximal spectral sensing to infer the relative abundances and spatial distribution of specific minerals associated with the surface-exposed alteration products typically found together with the Zn-Pb mineralization in carbonate-hosted and MVT systems. Several methods are proposed in order to determine the respective absorption feature characteristics from hyperspectral reflectance spectra (see the review by Laukamp et al., 2021). Nevertheless, the classification of hyperspectral images can be very challenging for several reasons, including data noise, high data dimensionality, and redundancy, as well as the presence of mixed pixels and limited availability of training samples (Kale et al., 2017). The feature-based band ratio approach (Laukamp 2022), instead, has several advantages. Firstly, it involves a small number of spectral bands, with the result that it is not computationally intensive. Secondly, it can be implemented following a transferable workflow for mapping lithology in almost all geological settings, and can be applied to all types of hyperspectral reflectance spectra that are collected by most of the imaging systems and sensors at different scales of observation, such as field spectrometers, drill core sensors, airborne sensors (e.g., HyMap, HyVista Corporation; AVIRIS, NASA/JPL) available on the market, and even some non-commercial spaceborne instruments (e.g., PRISMA, ASI; Hyperion), as in the present study.Table 1.

Alongside several papers focusing on the ASI's PRISMA hyperspectral sensor mission development, capabilities, performance analysis and potential uses and application fields (Amato et al., 2013; Pignatti et al., 2013; De Bonis et al., 2015; Loizzo et al., 2018; Cogliati et al., 2021; and references therein), recent works using PRISMA images mainly focused on first assessment of the potential of PRISMA for detecting and classifying vegetation, forest types, agricultural application, as well as land-use monitoring and hazard management (Pepe et al., 2020; Casa et al., 2020; Vangi et al., 2021). Other successful recent applications include water monitoring, as well as water quality assessment (Giardino et al., 2020; Niroumand-Jadidi et al., 2020). Only limited studies focus on lithological mapping (e.g., (Bedini and Chen 2020; Heller Pearlshtien et al., 2021, Laukamp, 2022). Geological applications of PRISMA images include till now: (1) the mapping of hydrothermal alteration assemblages; (2) delineating the spatial distribution of alteration minerals, for example, white micas associated with hydrothermal systems in the Cuprite area in Nevada, USA (Bedini and Chen 2020); (3) detecting CO_2 emissions (Romaniello et al., 2021; Romaniello et al., 2022); as well as (4) mapping methane emission points at upstream facilities of the oil and gas industry (Guanter et al., 2021). Heller Pearlshtien et al. (2021), instead, proposed a very detailed study based on the spectral performances of both Level 1 (L1 - radiance) and Level 2 (L2 - reflectance) PRISMA products over well-known geological features in the Makhtesh Ramon national park area in Israel. Specifically, the latter authors proceed by comparing hyperspectral PRISMA data to both AisaFENIX airborne hyperspectral and USGS spectral libraries data, demonstrating that PRISMA L1 products

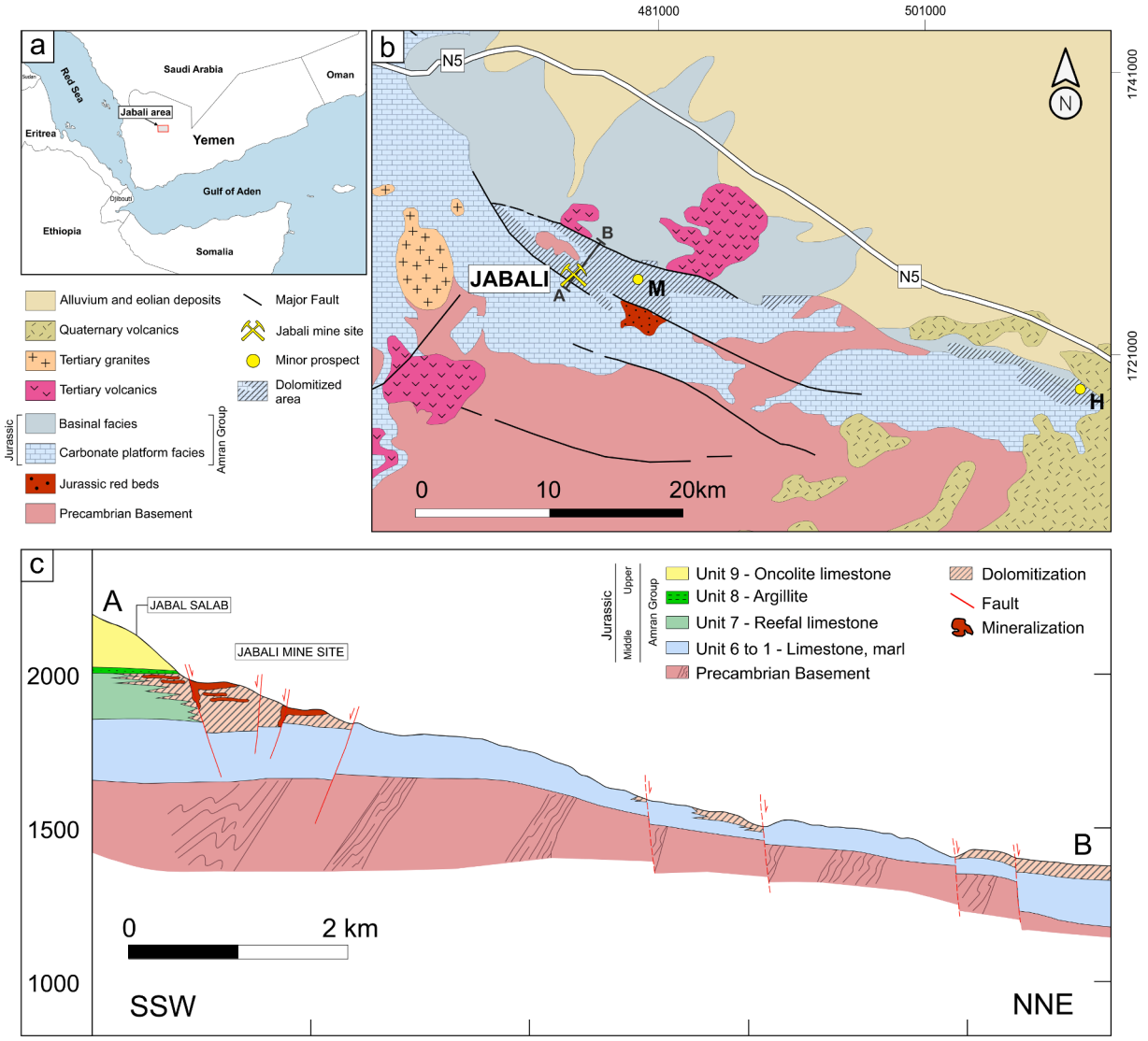

Fig. 1. (a) Location of the Jabali mine site; (b) Simplified geological map of the western portion of the Sab'atayn basin. The known Zn-Pb occurrences are highlighted. M: Majnah Ba, Pb, Zn mineralized zone; H: Jabal Haylan gossans. Modified from (Christmann et al. 1989). (c) Schematic NNE cross-section showing the mineralization and the Jurassic sequence in the study area (section trace is shown in Fig. 1B). Modified from (Christmann et al. 1989).

provide an accurate spectral-based mapping of minerals over the Makhtesh Ramon area. Heller Pearlshtien et al. (2021) produced good results especially for Fe oxy-hydroxides (goethite and hematite), gypsum and clay minerals, while L2D products showed inaccuracies due to noise and reflectance interference across the SWIR-2 long-wavelengths region. However, on the latest specific point, by using the mineral absorption feature-based band ratios method, Laukamp (2022) could successfully use the L2D PRISMA products, being able to map bedrock geology and regolith in Rocklea Dome, Western Australia, considering SWIR-2-active minerals, like: chlorite, epidote and other minerals.

The main aims of this study are to test the effectiveness of PRISMA as a tool for mineral exploration and to develop new workflows for identifying Zn-Pb mineralized areas. Specifically, we provide a new method for the extraction of mineralogical-chemical features related to carbonate-hosted and MVT ore deposits and related supergene alteration using PRISMA-derived data, in part interpreted by referencing field-based hyperspectral data. The method is focused on the depth of specific features, for the identification of ferric oxides- and carbonate-bearing rocks, which can be spectrally separated due to the main Fe^{3+}- and CO_3 ion-related absorption features in the VNIR and SWIR-2, respectively. Despite previous studies (e.g. Heller Pearlshtien et al., 2021) encountering problems in mapping carbonate phases using L2 PRISMA scenes, the method proposed in this study shows satisfactory results in mapping both limestones and dolomites.

The test area selected for this study is the Jabali district in Yemen. The district is situated about 110 km to the north-east of the capital city Sana'a, on the northwestern margin of the Sab'atayn sedimentary basin which hosts the main hydrocarbon resources in Yemen (Christmann et al., 1989; Al Ganad et al., 1994) (Fig. 1a). The district also includes the Jabali Zn-Pb deposit, which is one of the most important Zn-Pb-(Ag) deposit of the Arabian shield (Mondillo et al., 2014). The entire district was already field mapped by the Yemen Geological Survey (Christmann et al., 1989 and references therein). In addition, local spectral maps were produced using Landsat (MSS, TM, ETM +), QuickBird, and ALOS AVNIR-2 multispectral satellite data (Deroin et al., 2011, 2012), with satisfactory results in characterizing gossans and less accuracy with carbonate rocks. This information makes possible the validation of the PRISMA-derived maps at the district scale. For this study, a PRISMA level 2C (Bottom-Of-Atmosphere reflectance) datum was used for the detailed discrimination between distinct geological targets, since it covers at hyperspectral resolution at a sufficiently high signal-to-noise (SNR) ratio (Loizzo et al., 2018) for the wavelength

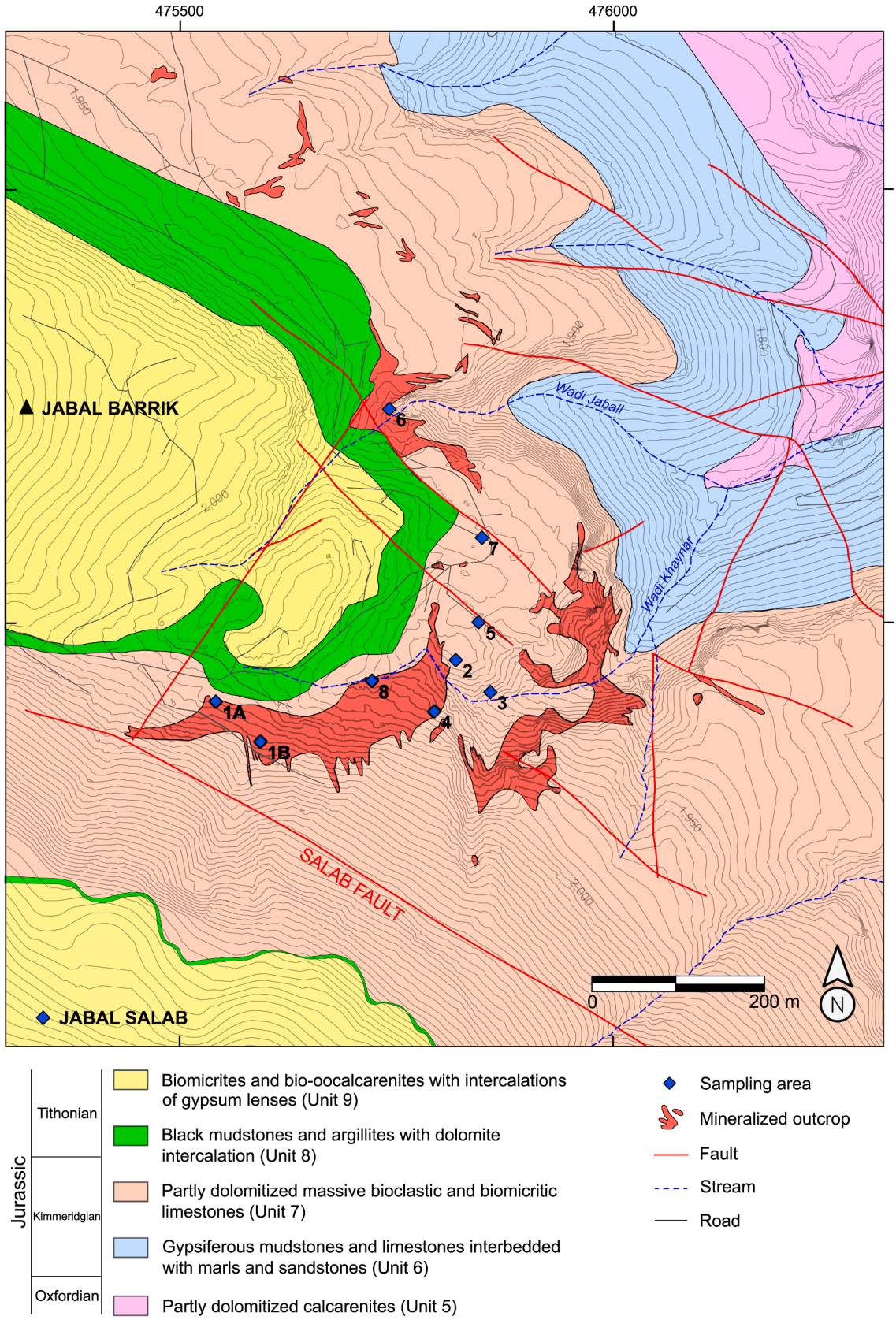

Fig. 2. Geological map of the Jabali mining site with the location of the analyzed samples (modified from Mondillo et al. 2014; Santoro et al. 2015; SRK Consulting, 2005).

regions diagnostic of the target minerals. Several ground samples from the Jabali deposit were characterized through the use of field reflectance spectroscopy, X-ray powder diffraction (XRPD) with Quantitative phase analysis (QPA), and whole-rock geochemical analyses (ICP-MS/ES), for better interpretation of the satellite hyperspectral data.

2. Geological setting

2.1. Regional geology

The Jabali ore deposit is located on the eastern flank of a local uplifted block, known as the Jabali-Majnah paleohorst, situated on the northwestern edge of the Late Jurassic-Early Cretaceous Marib-Al-Jawf/Sab'atayn basin (Fig. 1b). The Sab'atayn basin has a NW-SE orientation resulting from the development of extensional faults along the pre-existing Precambrian basement wrench-faults. It is mainly characterized by Mesozoic pre-, syn- and post-rift sedimentary sequences, represented by fluviatile red beds of the Kuhlan Formation and shallow marine carbonate sequences of the Amran Group, transgressive over the Precambrian metavolcanic and metasedimentary basement rocks, consisting of schists and quartzites intruded by granite and pegmatite (Al Ganad et al., 1994) (Fig. 1b, c). Tertiary alkaline granite bodies are present at Jabal as Saad, 15 km to the west of the Jabali mine site (Mondillo et al., 2014) (Fig. 1b). The Zn-Pb(-Ag) ores are mainly hosted by strongly dolomitized platform carbonates of the pre- to *syn*-rift Shuqra Formation (Amran Group, Jurassic) (As-Saruri et al., 2010; Mondillo et al., 2014; Santoro et al., 2015) (Fig. 1b, c; Fig. 2). Locally, the Shuqra Formation is subdivided into seven units (members), based on different sedimentological features (Al Ganad et al., 1994; Mondillo et al., 2014). Units from 1 to 6 are neiher mineralized nor dolomitized. Unit 7 appears almost completely dolomitized and is the main host for the Zn ores. The overlying Madbi Formation (0–30 m), locally called Unit 8, consists of organic-rich mudstones with gypsum and dolomite intercalations. The topmost Sab'atayn Formation, locally known as Unit 9, is characterized by biomicrites with oncolites and bio-oocalcarenites, as well as intercalations of gypsum lenses (Christmann et al., 1989) (Fig. 2). The sedimentary succession at Jabali is sub-horizontal, with just a few areas showing W-dipping strata. It is characterized mainly by brittle deformation related to extensional rift tectonics. The main normal fault system shows a NW-SE-strike (120° to 140°), dipping to the northeast, and can be observed bordering the plateau's southern side, below the Jabal Salab peak. Further sets of normal faults have 65° to 80° and 0° to 5° trends, while a minor fracture trend varies between 25° and 40° (Mondillo et al., 2014; SRK Consulting, 2005) (Fig. 2). Faults dip angles generally range between 60° and 80°.

2.2. Zn-Pb mineralization

The Jabali deposit represents the most prominent example of carbonate-hosted hydrothermal Ag-rich Zn-Pb mineralization of the Sab'atayn Basin (Christmann et al., 1989; McCombe et al., 1994; Ostendorf et al., 2015). The estimated resources of 12.6 Mt at 8.9 % Zn, 1.2 % Pb, and 68 mg/kg Ag (SRK Consulting, 2005) are characterized by Zn-oxidized minerals (also called "nonsulfides"), derived from the alteration of preexisting Zn sulfides (Mondillo et al., 2014, 2011; Ostendorf et al., 2015). The orebodies in part outcrop at the surface in the form of Fe-oxy-hydroxides-rich gossans and nonsulfides derived from supergene alteration (Figs. 1c and Fig. 2), with many more present in the subsurface below Jabal Barrik (Mondillo et al., 2014; Santoro et al., 2015). The orebodies are either stratabound following the dolostone layering or structurally controlled along vertical fractures, faults, and fault intersections (Al Ganad et al., 1994; Mondillo et al., 2014). Primary sulfide mineralization, consisting of sphalerite, galena and pyrite, has been preserved locally in intervals underlying the Madbi Formation (Unit 8; Fig. 1c) and corresponds to a Late Jurassic extensional MVT (Al Ganad et al., 1994; Mondillo et al., 2014; Ostendorf et al., 2015). Two distinct dolomite generations have been observed within the study area (Al Ganad et al., 1994; Mondillo et al., 2014): (1) an early district-scale diagenetic dolomite and, (2) a hydrothermal dolomite, genetically associated with Zn-Pb sulfide deposition. The latest consists of Fe-Mn-bearing saddle crystals (FeO up to 6 wt% and MnO up to 2 wt %) (Mondillo et al., 2014) occurring as geodes, veins, and replacing the former diagenetic generation. The ore-related hydrothermal dolomite bodies are mainly controlled by porosity and fractures, following the main N120° to N140° structural trend observed in the area (Christmann et al., 1989) (Fig. 1c and 2). Both the dolomite generations are affected by two different alteration/replacement processes: (1) de-dolomitization, occurring as calcite formation by replacement of the former dolomite crystals, as well as Fe^{2+} altered to Fe^{3+} reprecipitating in form of Fe^{3+}-hydroxides in the interstices of the crystals and pores; (2) dolomite replacement by Zn-bearing dolomite (17–22 wt% ZnO) (Mondillo et al., 2011, 2014; Santoro et al., 2015), where Zn^{2+} replaces Mg^{2+} in the dolomite as a consequence of interaction with Zn-enriched groundwaters after sulfides alteration processes, and formation of Fe-hydroxides due to the release of Mn^{2+} and Fe^{2+} after oxidation. The oxidized mineralization at Jabali consists of massive to semi-massive and disseminated orebodies of nonsulfide mineral aggregates (Mondillo et al., 2011, 2014; Santoro et al., 2015). Smithsonite represents the main economic mineral and is associated with minor hemimorphite and hydrozincite, with disseminated Ag-sulfides. Smithsonite replaces both sphalerite and all the dolomite phases described above (Mondillo et al., 2014). It is suggested that the oxidized mineralization formed since the early Miocene (~17 Ma) after the alteration of preexisting sulfides due to the action of supergene waters mixed with low-temperature hydrothermal fluids (Mondillo et al., 2014).

3. VNIR and SWIR absorption features of minerals investigated in carbonate-hosted Zn-Pb deposits

The spectral range between 400 nm and 2500 nm (VNIR to SWIR) characterizes many hydrothermal and supergene minerals in terms of spectral responses, allowing their identification when they are considered as target minerals. Displacements of the absorption feature to either longer or shorter wavelengths can highlight either mineral compositional variations or mineral mixing, whereas absorption band depth (relative to the background continuum) can be assumed to be proportional to the mineral relative abundance (Clark et al., 1990). Reference spectral reflectance features of the main host-rock and supergene alteration minerals observed in the Jabali samples are shown in Table 1. Two main processes cause the mineral-related absorption features in the SWIR 2 range (Laukamp et al., 2021): (1) combinations (ν + δOH) of hydroxyl-related fundamental stretching (νOH) and bending vibrations (δOH), and (2) combinations (e.g., $2\nu_3 + \nu_1$ CO_3) or overtones (e.g., $3\nu_3CO_3$) of carbonate-related fundamental stretching vibrations. Several authors have comprehensively studied the spectral properties of carbonates (Hunt and Salisbury 1971; Gaffey 1985, 1986; Crowley 1986; Clark et al., 1990; Van der Meer 1995; Kurz et al., 2012; Zaini et al., 2012; Green and Schodlok 2016; Laukamp et al., 2021). As a general rule, carbonate minerals can be distinguished in the SWIR by the presence of two main spectral absorption features in the wavelength regions around 2300–2350 nm and 2500–2550 nm (Hunt and Salisbury 1971; Gaffey 1986; Clark et al., 1990; Zaini et al., 2012), the latter of which is generally placed at the boundary of the wavelength ranges acquired by the most common hyperspectral instruments. In this context, the main absorption feature considered ($3\nu_3CO_3$) for calcite occurs in the 2335–2340 nm wavelength region. Several factors control the position of carbonate absorption bands at the atomic level (e.g., cation mass, cation radius, cation and anion valences, cation coordinate number, the gap between cation and anion, and site symmetry), as well as physical and chemical properties (i.e., grain size, texture, packing or porosity, carbonate mineral content, chemical composition). The grain size has effects on the absolute reflectance values (band absolute depth), but

absorption feature position, width and asymmetry are not significantly affected either by grain size or packing in the SWIR wavelength region (Gaffey 1986; Zaini et al., 2012). The quantity of metal cation (Mg, Fe, and Mn replacing Ca) bonded to the CO_3^{2-} in the crystal lattice and the relative amounts of carbonate phases composing the samples, instead, can control the wavelength position and the geometry of such absorption features (Hunt and Ashley 1979; Gaffey 1986; Laukamp et al., 2021), therefore positions of the main carbonate absorption features can shift with changes in chemical composition, proportionally with the amount of metal cation replacing Ca (Gaffey 1985, 1986). Thus, the main CO_3^{2-} absorption appears shifted to shorter wavelengths for dolomites, with the main feature occurring at 2320 nm. The latter property is generally used as a diagnostic feature to make a distinction between limestone and dolomite (Clark et al., 1990; Kurz et al., 2012; Van der Meer, 1995; Windeler and Lyon, 1991). Moreover, the main absorptions appear asymmetric with a shoulder on the short-wavelength side (Gaffey 1985, 1986), pointing to a secondary weaker absorption probably centered in the 2230–2275 nm range (Laukamp et al., 2021). Increasing Fe content can cause carbonate bands in dolomite and calcite spectra to shift to longer wavelengths, associated with broad double bands centered near 1200 nm and 1300 nm, respectively, attributed to electronic transitions of the Fe^{2+} ion (Crystal Field Absorption band - CFA). Furthermore, an increase in the intensity of this feature was observed in association with increasing iron content in dolomites and calcites (Gaffey 1986). However, the strength of the Fe^{2+} CFA feature was found to be very variable, especially when comparing it across mineral species (Hunt and Salisbury 1971; Gaffey 1986; Green and Schodlok 2016; Lampinen et al., 2019). Two less intense diagnostic absorption features in calcite occur at around 1990 nm (medium intensity) and 1870 nm (weak intensity), respectively. The intensity of these absorption features decreases with increasing Mg or Fe content. However, because they overlap with the main OH/H_2O absorption at around 1900 nm, these features can be obliterated, becoming not useful for satellite-based hyperspectral analyses. According to Laukamp et al. (2021), they can help when the true nature of a left-hand asymmetric absorption feature in the 2340-nm region is dubious.

The Zn carbonates smithsonite ($ZnCO_3$) and hydrozincite ($Zn_5(CO_3)_2(OH)_6$) show the carbonate absorption features in the range between 2300 nm and 2400 nm (McConachy et al., 2007). The main CO_3^{2-} absorption band for smithsonite is present at 2365 nm, whereas hydrozincite absorptions occur as only minor absorptions at 2300 nm and 2400 nm. Smithsonite can change in color from white to brown–red varieties. The brown–red variety shows deep and broad crystal field effects, due to Zn^{2+} between 800 nm and 1200 nm, centered around 960 nm (McConachy et al., 2007).

H_2O and/or OH-bearing Zn silicates, such as hemimorphite ($Zn_4Si_2O_7(OH)_2H_2O$) and sauconite ($Na_{0,3}Zn_3(Si, Al)_4O_{10}(OH)_2(H_2O)$), are characterized by significant absorption features close to 1400 nm and 1900 nm, caused by the first overtone of O—H stretching vibration and the combination of O—H stretching and H—O—H bending vibrations, respectively (Hunt 1971; Hunt and Salisbury 1971; Crowley 1991; McConachy et al., 2007). Nevertheless, these features are not useful for satellite-based hyperspectral analyses, because of atmospheric interferences. Weaker absorption bands in the SWIR region, instead, are related to Zn–OH, occurring at 2210 nm for hemimorphite and 2305 nm for sauconite. Si–O bonding appears very weak in the SWIR (McConachy et al., 2007).

Iron-bearing oxides/hydroxides (i. e. hematite and goethite; Crowley et al., 2003; Cudahy and Ramanaidou, 1997; Curtiss, 1985) are defined by diagnostic absorption features in the range between 450 nm and 1200 nm, corresponding to the VNIR region of the electromagnetic spectrum. The significant absorption bands of these phases are caused by electronic processes involving Fe^{3+} octahedrally bonded to ligands of oxygen (hematite α-Fe_2O_3) or oxygen and hydroxyl (goethite – α-FeO(OH)) (Cudahy and Ramanaidou 1997). In detail, hematite exhibits its diagnostic absorption feature typically at ~ 880 nm, which is related to energy level changes in the valence electrons (CFA). The major CFA feature of goethite appears, instead, shifted to longer wavelengths compared to hematite, occurring generally at ~ 940 nm (Cudahy and Ramanaidou 1997; Crowley et al., 2003). Other weaker absorption bands are at 480 nm and 670 nm (Charge Transfer Feature – CTF; Cudahy and Ramanaidou 1997), and the water-related features are close to 1400 nm and 1900 nm. Absorption position shifting to longer wavelengths of the main Fe-bearing oxides/hydroxides feature (of about 14 nm; Scheinost et al., 1999) is due to compositional modifications related to Al^{3+} substitution for Fe^{3+} iron (Cudahy and Ramanaidou 1997). As a common product of supergene alteration of sulfides ores, jarosite ($KFe_3(SO_4)_2(OH)_6$) can show the CFA absorption features at ~ 910 nm and ~ 437 nm, together with the weaker 650 nm band (Crowley et al., 2003). Moreover, jarosite (as well as plumbojarosite) shows OH-related features at around 2212 nm and 2263 nm, which it shares with di-octahedral and tri-octahedral sheet silicates, respectively (Bishop and Murad 2005; Laukamp et al., 2021).

Di-octahedral sheet silicates (white micas, Al-smectites, and kaolinite) are SWIR 2-active mineral phases, producing a characteristic Al-OH spectral absorption feature between 2195 and 2225 nm. The absorption is related to the presence of hydroxyl bound to Al (Al-OH) in the octahedral layer, and it is given by the combination of the Al-OH bending and the O—H stretching vibration ($\nu + \delta Al_2OH$; (Vedder and McDonald 1963; Vedder 1964; Hunt 1977; Clark et al., 1990; Van der Meer 2004; Laukamp et al., 2021).

The O—H—related absorption feature in white micas is centered at around 2350 nm, overlapping the carbonate spectral feature in the same range from 2300 to 2550 nm (Clark et al., 1990; Van der Meer 2004). As noted earlier, the left-hand symmetry shown by the spectral absorption feature at 2300 to 2335 nm, can be used to distinguish them from white micas (Gaffey 1986; Lampinen et al., 2017).

4. Materials and methods

4.1. Analysis of ground samples

For this study, 17 ground samples (carbonate host-rock and Fe- and Zn-bearing mineralized products) from 10 sampling areas in the Jabali mine site were analyzed (Fig. 2). VNIR-to-SWIR reflectance spectra were measured in the laboratory at CSIRO Mineral Resources (Perth, Western Australia), focusing on both fresh and altered portions, using a FieldSpec Pro 3 spectrometer, which records spectra via contact probe, with a data acquisition spot size of 10 mm, and a spectral resolution of 10 nm with a sampling interval of 1 nm in the 350- to 2500-nm wavelength range (https://www.malvernpanalytical.com/). Acquired hyperspectral data were downsampled using ENVI 5.6.1 software (L3Harris Technologies, USA) to the PRISMA resolution (see Cogliati et al., 2021 for specifications), to test the effect of spectral resolution on the measuring and mapping of the abundance and composition of specific minerals. The Spectral Library Resampling tool in ENVI was used for downsampling the field-based spectral library by applying a Gaussian model proving wavelengths (band centers) and full-width-half-maximum (FWHM) information obtained from the PRISMA input data file.

Spectra display, analysis and interpretation were carried out using The Spectral Geologist software (TSG™ version 8.0.7.4, CSIRO, Perth, WA, Australia, https://research.csiro.au/thespectralgeologist, accessed on 25 November 2021). Since the characteristics of the absorption features of the mineral phases of interest (summarized in Table 1) can be extracted from reflectance spectra through band ratios or polynomial fitting, the spectra analysis was performed by plotting the relative intensities of each diagnostic absorption feature obtained by feature extraction scripts, then shown in binary discrimination diagrams. We used the feature extraction scripts derived from previous work by (Cudahy et al., 2008) and (Laukamp et al., 2011, 2021; Lampinen et al., 2019), that were adapted to the PRISMA bands setting and applied to reflectance spectra downsampled to the PRISMA spectral resolution,

Table 2
Indices (in italic) used for identification of the various mineral groups and mineral phases based on their absorption features in the VNIR and SWIR regions, and their applicability. The stretch values give the lower and upper limits applied to the respective index for the PRISMA mineral maps.

Index name	Index Identifier	Applicability	Algorithm	PRISMA algorithm	Stretch lower limit*	Stretch upper limit*	References
Mg-OH feature depth	*2350D*	Abundances of both carbonates (e.g., calcite, dolomite) and trioctahedral silicates (e.g., chlorite, epidote, amphibole, talc, FeMg-clays).	(R2327 + R2364)/ R2349	*(B149 + B154)/B152*	1.97	2.12	Laukamp et al. (2011)
Al-sheetsilicate feature depth (ASA)	*2200D*	Abundance of white micas (e.g. illite, muscovite, paragonite, brammalite, phengite, lepidolite, margarite) and smectites (montmorillonite, beidellite)	(R2143 + R2229)/ R2206	*(B125 + B136)/ B133; masked with 2350D < 2.0*	2.15	2.32	Laukamp (2022); Sonntag et al. (2012)
Dolomites feature depth	*2320D*	Abundance of dolomites	(R2298 + R2342)/ R2320	*(B145 + B151)/B148*	2.08	2.15	Gaffey (1986); Laukamp et al. (2012)
Fe (oxyhydr-) oxides abundance (FOA)	*900D*	Abundance of mixture of hematite, goethite, "limonite", ferrihydrite, jarosite, Fe^{3+}-carbonate	(R770 + R962)/R908	*(B44 + B62)/B57, masked with 2350D < 2.0 and 2200D > 2.15*	2.3	2.4	Cudahy et al. (2008); Haest et al. (2012a, 2012b); Laukamp (2022)

after continuum removal by division of the reflectance spectrum by the continuum. For extraction of the relative abundance of a given mineral, the sum of two spectral bands located at the shoulders of a given absorption feature is divided by one or more bands located at the center of the absorption minimum. The binary diagrams are useful to identify clusters of mineral species or groups characterizing the analyzed samples, to evaluate their spectral behavior, and, amongst other applications, to estimate relative mineral abundances and compositional changes. The feature extraction indices description is shown in Table 2. We firstly focused on the SWIR 2 wavelength region (between 2000 and 2500 nm) by using the *2320D* and *2350D* feature extraction scripts, plotted against the Carbonate Composition script (Sonntag et al., 2012). The VNIR region, instead, was considered for evaluating the Ferric Oxide Abundance, applying the same-named feature extraction script (hereinafter referred to as *900D*), plotted against the Hematite-Goethite ratio (Cudahy and Ramanaidou 1997; Cudahy et al., 2008). The authors decided to keep the same nomenclature adopted in previous studies, labeling the latter scripts by the center wavelength position followed by D (for "depth") (Laukamp et al., 2021).

To validate the laboratory reflectance hyperspectral measurements, X-ray powder diffraction (XRPD) and Quantitative phase analysis (QPA) were conducted on the 17 milled samples (Table 3), corresponding to the half counterparts of the samples used for spectral analysis. An aliquot of 20 wt% corundum was added to the powders to quantify mineral and amorphous contents. The XRPD analyses were conducted at the Osservatorio Vesuviano-INGV (Napoli, Italia) with a Panalytical X'pert PRO PW 3040/60 Malvern- Panalytical diffractometer in Bragg-Brentano geometry with unfiltered CuKα radiation (40 kV, 40 mA) in the 3°-70° 2θ range, in steps of 0.02° 2θ, counting time in 30 s/step. Diffraction patterns were interpreted using the HighScore software version 4.9 (Malvern Panalytical B.V.) and JCPDS PDF-2 database. QPA followed the combined Rietveld and Reference Intensity Ratio (RIR) methods (Chung 1974a, b; Bish and Post 1993; Gualtieri et al., 1996; Gualtieri 2000). The profile was refined using the High Score plus 4.9 software exporting the structure models for each phase from ICSD data library. Rietveld refinement has been performed by correcting major parameters like scale factor, flat background, zero shift, lattice parameters, half-width, orientation parameters, U V W, peak shape parameters, etc., to obtain high Goodness of Fitment (GOF) and reliable Rwp and Rp agreement indices. Bulk-rock geochemical analyses (Table 4) were used to better evaluate compositional variations characterizing the samples, to calibrate the XRPD analyses (see for example Santoro et al., 2021), and for comparison with the reflectance spectroscopic data. Ten grams of identical split powders to those used for the XRPD analyses were used for determining major, minor, and trace element concentrations by Bureau Veritas Commodities Canada ltd. (Vancouver, Canada). Major oxides were analyzed by Inductively Coupled Plasma Emission Spectroscopy (ICP-ES) and Trace Elements by Inductively Coupled Plasma-Mass Spectroscopy (ICP-MS), following a lithium borate fusion on the LF202 package, in which the samples are fused with Li_2B4O_7/ $LiBO_2$ fluxes before being analyzed by ICP-ES/MS. Fe^{2+} was analyzed using the GC806 package (FeO Titration). Zn and Pb over limits were analyzed by GC816 (Zn Titration) and GC817 (Pb Titration), respectively.

4.2. Satellite hyperspectral data collection and processing

The mineral maps presented in this article are based on a Bottom-Of-Atmosphere (BOA) reflectance hyperspectral satellite image using the PRISMA hyperspectral satellite sensor, which is currently acquiring data all over the World, releasing free images to scientific community and the public. The hyperspectral datum (PRS_L2C_STD) was acquired at 07:41:46 a.m. on 21 November 2021 (UTC) and downloaded from the mission website (www.prisma.asi.it; accessed on 21 November 2021) (Fig. 3). The L2 PRISMA products are atmospherically corrected images following the standard data processing chain developed by ASI for PRISMA (see PRISMA product specifications, www.prisma.asi.it). PRISMA consists of a 5 m resolution co-registered panchromatic camera and a push-broom hyperspectral imaging spectrometer. The hyperspectral camera acquires a continuum of 234 spectral bands at a spatial resolution of 30 m on a swath of 30 km, and spectral resolution ranging from 11 to 15 nm from the VNIR to the SWIR wavelength regions (Agenzia Spaziale Italiana (ASI), 2020; Cogliati et al., 2021; Loizzo et al., 2018). The PRISMA data are filed in HDF-EOS5 format (Hierarchical Data Format - Earth Observing System) and comprehend the panchromatic (PAN), VNIR, and SWIR datasets (Fig. 4).

The workflow proposed for this study (Fig. 4) was performed using a range of tools in ENVI 5.6.1. At first sight, PRISMA hyperspectral bands strongly affected by atmospheric absorption were excluded from further processing. Atmospheric absorption bands occur in the wavelength ranges between 1317 and 1533 nm and 1784 to 2035 nm, corresponding to the band ranges from B39 to B59 and from B84 to B112, where B is used to indicate spectral bands of the PRISMA SWIR cube. Due to their low SNR, SWIR bands from B158 (2392 nm) to B173 (2495 nm) were not considered. Errors in the absolute geolocation of ~ 100 m of the L2D PRISMA images introduced issues in the comparison with field hyperspectral data. However, the geolocation was improved using the Refine RPCs (HDF-EOS5) task, contained within the PRISMA Toolkit, a recently developed extension for ENVI. The task relies on a Sentinel-2 reference image with the same acquisition date, which has geometric localization errors not >5 to 10 m (European Space Agency, 2015). Cross-track illumination correction (using a sample-based approach) was applied

Table 3
Mineral abundances (wt.%) from X-ray diffraction quantitative analysis of outcrop samples.

Sample ID	Sampling area	Sample group	Dol	Cal	Hm	Hyd	Sm	Qz	Gth	Hem	Sme	Jrs	Pb-Jrs	Kln	Ilt	Gp	Cph	A-FeHyOX	TOT
JSMAR4	8	Zn ore	72		3	20.2					0.8						1.3	2.7	100
JSMAR5	2	Zn ore	24	54.8	2.9		8	1			0.2							9.1	100
JSMAR7	7	Gossan		64.5					31			0.5		tr.				4	100
JSMAR8	7	Zn ore		6.9	23.2	56.9	5											8	100
JSMON H9		Host rock		96.1														3.9	100
JSMON13	1B	Zn ore	34.5				55.7		1.5		1			tr.				7.3	100
JSMON16	2	Gossan		43				1.3	20.7	13.2								21.8	100
JSMON18	3	Gossan		18.8			14.6	3.6	6.1	23.2	8		16.5			0.2	1.3	23.6	100
JSMON2	1 A	Host rock	72.5	7			4.6		4									0.6	100
JSMON20	3	Zn ore			14.5	19.1			40.4									21.4	100
JSMON23	4	Host rock	87	1					1.7		2							8.3	100
JSMON25	4	Gossan		26.7					47.5									25.8	100
JSMON29	5	Zn ore			8.5	77.6	2.2				2.5							9.2	100
JSMON31	5	Gossan		1					61.3	15.4					1.3			21	100
JSMON33	6	Host rock	74.5	14.9							4.5							6.1	100
JSMON39	Jabal Salab	Gossan		34.5					49.2									16.3	100
JSMON3b	1 A	Host rock	88.5	4.8			0.7							tr.				6	100

Notes: The sampling areas location is indicated in Fig. 2. Abbreviations mostly after Mondillo et al. (2014) - Dol: dolomite; Cal: calcite; Hm: hemimorphite; Hyd: hydrozincite; Sm: smithsonite; Qz: quartz; Gth: goethite; Hem: hematite; Sme: smectites; Fld: feldspar; Jrs: jarosite; Pb-jrs: plumbojarosite; Kln: kaolinite; Ilt: Illite; Gp: gypsum; Cph: chalcophanite; A-FeHyOX: Amorphous Fe-hydroxides.

to both VNIR and SWIR scenes, before stacking them to investigate the full wavelength range as determined by target minerals' significant absorption features. The latter correction was applied to reduce the "see-saw" pattern in the VNIR wavelength range that is caused by the applied spectral resampling during the smile correction processing within the L1 processor (Cogliati et al., 2021). The product's stacking was performed using the Build HSI Cube task, included in the PRISMA Toolkit in ENVI, which allows the combination of the VNIR and SWIR datasets and the removal of the redundant overlapping wavelengths. The final processed product includes only 168 bands out of 234 original bands. The stacked product was smoothed before further processing, using the Savitzky-Golay smoothing filter in ENVI (Savitzky and Golay 1964). The best results were obtained by using a combination of filter parameters including Filter Width = 3, Order of the Derivative = 0, and Degree of Smoothing Polynomial = 2. Pixel affected by shadows or belonging to non-geological materials, mainly vegetation and man-made features, were masked and excluded as well. The vegetation and agriculture areas masking carried out using the Normalized Difference Vegetation Index (*NDVI*), that for the PRISMA specific case is (*B53-B35*)/(*B53* + *B35*), where band 35 (RED) is centered at 679.48 nm, while band 53 (NIR) corresponds to 865.95 nm ("*NDVIcsiro*"; Laukamp et al., 2022) with *NDVIcsiro* > 0.13 masked out. Other interference factors (e.g., roads, the nearby exploration camp, bare areas under cultivation) were recognized visually, supported by higher spatial resolution satellite images and local large-scales maps, then masked using specifically designed *Regions of Interest* (ROIs), and excluded from further processing. Finally, a spatial subset was obtained before the mineral mapping.

4.3. Hyperspectral mineral mapping

The feature extraction indices technique adopted in this study assumes that the combination of a relatively small number of bands (wavelength) can outline the interaction between light and surface-exposed materials, extracting the wavelength position of specific absorption features exhibited by rock-forming and alteration minerals, regardless of the number of bands collected (Laukamp et al., 2021). Therefore, feature extraction indices were applied to the PRISMA L2C subset scene for obtaining surface compositional information, while at the same time minimizing reflectance variations associated with topography and albedo effects (Crowley et al., 1989; Clark et al., 1990). The band ratios used were adapted to the PRISMA hyperspectral data, avoiding bands dominated by strong instrument noise, to minimize along-track striping and improve contrast of the remaining pixel values. The considered feature extraction indices can be easily applied by using the Band Algebra Tool in ENVI.

We focused on interpreting/discriminating the dolomitization distribution in the Jabali area, mainly using the following band ratios (Table 2):

$$2320D = \frac{R2298 + R2342}{R2320} = \frac{\mathrm{B145} + \mathrm{B151}}{\mathrm{B148}} \quad (1)$$

$$2350D = \frac{R2327 + R2364}{R2349} = \frac{\mathrm{B149} + \mathrm{B154}}{\mathrm{B152}} \quad (2)$$

where R is the reflectance value and B is the corresponding PRISMA spectral band (Gaffey 1986; Laukamp et al., 2012; Haest et al., 2012a, b). The *2320D* index was obtained by dividing spectral bands indicating the specific dolomites and limestones absorption minima. The algorithm is referred to the depth of the dolomites' diagnostic absorption at 2320 nm. The index *2350D* was introduced because the (1) output appears noisier. The index (2) is based on the 2349 nm feature. In the latter case, problems in delineating the dolomite distribution may arise when Mg-OH and Al-OH minerals-bearing rocks are also present because they are characterized by the 2350 nm absorption feature, which overlaps the absorption caused by carbonates. Since distinction from these other minerals can be achieved by other features, e.g., the Al- di-octahedral

Table 4
Major (wt.%) and minor (mg/kg) element concentrations of outcrop reference samples from ICP-ES/MS analysis.

	Sample ID	MDL	JSMAR4	JSMAR5	JSMAR7	JSMAR8	JSMON H9	JSMON13	JSMON16	JSMON18	JSMON2	JSMON20	JSMON23	JSMON25	JSMON29	JSMON31	JSMON33	JSMON39	JSMON3b
Wt%																			
SiO_2	LF200	0.01	1.15	1.96	0.82	7.6	0.64	1.14	2.76	8.08	0.54	4.43	1.35	2.1	2.64	2.03	1.94	2.58	0.62
Al_2O_3	LF200	0.01	0.17	0.2	0.22	0.48	0.07	0.25	0.52	4.59	0.05	0.23	0.4	0.41	0.3	0.58	0.83	0.5	0.22
Fe_2O_3	LF200	0.04	2.3	6.3	28.25	4.51	0.34	6.55	43.31	49.89	3.65	50.88	6	55.88	5.83	78.95	3.94	52.86	2.58
MgO	LF200	0.01	14.97	4.98	0.09	0.14	0.25	7.31	0.27	0.27	15.14	0.09	18.23	0.32	0.14	0.04	15.48	0.24	18.59
CaO	LF200	0.01	23.86	37.33	36.04	3.31	54.73	10.83	23.95	10.59	26.14	0.13	27.55	14.72	0.36	0.56	30.44	19.19	30.04
Na_2O	LF200	0.01	0.05	<0.01	<0.01	0.02	<0.01	<0.01	0.03	0.04	0.01	0.04	<0.01	0.02	0.07	0.18	<0.01	0.01	0.02
K_2O	LF200	0.01	0.02	<0.01	<0.01	<0.01	0.01	<0.01	0.04	0.09	<0.01	0.02	0.03	0.02	0.03	0.13	0.02	0.02	0.03
TiO_2	LF200	0.01	<0.01	<0.01	0.02	0.02	<0.01	0.01	0.1	0.05	<0.01	0.02	0.03	0.04	0.02	0.26	0.06	0.02	0.02
P_2O_5	LF200	0.01	<0.01	0.04	<0.01	0.02	0.01	0.03	0.02	0.11	<0.01	0.03	0.01	0.02	<0.01	0.11	0.03	0.03	0.02
MnO	LF200	0.01	0.89	0.86	0.04	2.22	0.14	1.11	0.05	0.73	0.91	0.06	0.66	0.04	0.99	0.07	0.79	0.04	0.79
FeO	GC806	0.2	<0.20	<0.20	<0.20	<0.20	<0.20	<0.20	0.35	<0.20	<0.20	<0.20	<0.20	<0.20	<0.20	<0.20	<0.20	0.31	1.89
ZnO	GC816*	1	17.54	10	<1.00	59.3	–	37.48	1.97	3.72	10	29.23	3	3.51	65.7	3.01	3.5	1.33	–
PbO	GC817*	2	–	–	<2.00	–	–	–	3.23	6.03	–	–	–	<2.00	–	<2.00	–	<2.00	–
Cr_2O_3	LF200	0	<0.002	<0.002	<0.002	<0.002	<0.002	0	0	0.01	<0.002	0	<0.002	0	<0.002	0.01	<0.002	0.01	<0.002
LOI	LF200	–	41.1	38.9	33	20.7	43.7	36.3	24.1	15.4	43	16.1	43.5	21.2	24	13.9	42.9	23.1	46
TOT/C	TC000	0.02	10.87	10.37	8.26	3.46	12.03	9.95	5.55	2.36	11.93	1.54	11.71	3.55	4.07	0.29	11.55	4.25	12.75
TOT/S	TC000	0.02	<0.02	<0.02	0.06	<0.02	<0.02	<0.02	0.19	1.08	<0.02	0.16	<0.02	0.14	0.03	0.18	0.14	0.14	0.02
mg/kg																			
Ba	LF200	1	30	12	4	27	215	14	46	51	29	3	315	12	144	13	71	29	4
Ni	LF200	20	33	<20	<20	<20	<20	125	<20	78	<20	37	<20	21	<20	<20	<20	<20	<20
Sc	LF200	1	<1	1	<1	<1	<1	<1	1	7	<1	<1	<1	<1	<1	2	1	<1	<1
Be	LF200	1	<1	<1	<1	<1	<1	2	<1	4	<1	1	<1	<1	1	<1	<1	<1	<1
Co	LF200	0.2	1.2	2.8	0.4	33.3	0.3	9.5	1.5	26.7	0.9	1.5	0.8	1.1	21.8	0.8	2.6	2.5	1
Cs	LF200	0.1	<0.1	<0.1	<0.1	<0.1	<0.1	<0.1	<0.1	<0.1	<0.1	<0.1	<0.1	<0.1	<0.1	<0.1	<0.1	<0.1	<0.1
Ga	LF200	0.5	<0.5	5.2	0.7	1.2	<0.5	<0.5	14.5	21.7	1	<0.5	0.7	11.1	<0.5	5.2	1	3	<0.5
Hf	LF200	0.1	<0.1	0.1	0.2	0.1	<0.1	<0.1	0.9	0.6	<0.1	0.2	0.3	0.4	0.2	1.7	0.3	0.2	0.4
Nb	LF200	0.1	0.3	0.3	0.4	0.4	0.1	0.2	2.1	1.3	0.2	0.5	0.7	0.7	0.3	6.1	1.2	0.5	0.4
Rb	LF200	0.1	<0.1	0.2	0.1	<0.1	0.4	0.1	1.1	0.7	0.1	<0.1	1.2	0.1	<0.1	0.5	0.8	0.5	1
Sn	LF200	1	<1	1	<1	<1	<1	<1	5	6	<1	<1	<1	5	<1	<1	<1	<1	<1
Sr	LF200	0.5	34.2	106	24.1	13.8	78.7	32.3	397	175.4	19.8	6.8	53.7	21.6	15.5	22.9	86.3	178	48.3
Ta	LF200	0.1	<0.1	<0.1	<0.1	<0.1	<0.1	<0.1	<0.1	<0.1	<0.1	<0.1	<0.1	<0.1	<0.1	0.3	<0.1	<0.1	<0.1
Th	LF200	0.2	<0.2	<0.2	0.3	<0.2	<0.2	<0.2	0.7	1.8	<0.2	<0.2	0.5	0.6	0.2	1.1	0.7	0.5	0.2
U	LF200	0.1	1.7	3.2	2.8	11.8	1	1.3	4	10.9	0.8	2.4	1.6	3	2.8	5.3	2.7	3.8	1.3
V	LF200	8	10	8	<8	13	<8	9	<8	35	<8	<8	17	<8	<8	13	16	<8	8
W	LF200	0.5	<0.5	<0.5	<0.5	<0.5	<0.5	<0.5	0.6	<0.5	<0.5	<0.5	<0.5	<0.5	<0.5	0.9	0.8	<0.5	<0.5
Zr	LF200	0.1	2.1	9.3	6.9	7.6	3.9	3.3	35.5	21.4	3.3	6.6	11.4	15.4	6.5	65.9	12	10.3	25
Y	LF200	0.1	13	23	3.2	10.8	3.3	9.2	3.1	16.8	4.4	4.7	10.3	1.5	5.8	3.3	13.9	4.3	5.2
La	LF200	0.1	8.3	9.3	5	6.3	3	6.8	2.5	17.4	4.2	3	12.2	1.7	5.5	5.1	21.9	4.4	7.9
Ce	LF200	0.1	6.1	9.1	6.5	19	2.9	8.7	4.6	69.4	4.6	3.4	15	2	14.2	8.5	24.5	7	8.2
Pr	LF200	0.02	1.7	1.9	1.1	1.5	0.5	1.2	0.5	3.5	0.6	0.6	1.9	0.2	1.6	0.7	2.9	0.8	1
Nd	LF200	0.3	7.7	8.7	4.4	6.6	1.9	4.5	2.2	16.3	2.5	3.1	7.3	0.9	7.5	2	11.1	3.4	4.2
Sm	LF200	0.1	1.4	2.2	0.9	1.5	0.3	0.8	0.6	5.6	0.5	0.5	1.4	0.2	1.6	0.3	2.2	0.6	0.7
Eu	LF200	0.02	0.5	1.5	0.3	0.9	0.1	0.4	0.2	1.8	0.4	0.3	0.9	0.1	0.7	0.1	1.8	0.2	0.5
Gd	LF200	0.1	2	3.3	0.8	2.2	0.4	1.2	0.6	6.5	0.7	0.7	1.8	0.3	1.5	0.3	3.1	0.8	0.9
Tb	LF200	0.01	0.2	0.5	0.1	0.3	0.1	0.2	0.1	1	0.1	0.1	0.2	0	0.2	0.1	0.3	0.1	0.1
Dy	LF200	0.1	1.4	3.3	0.4	1.6	0.4	0.8	0.5	5.6	0.4	0.6	1.1	0.2	1.1	0.4	1.5	0.6	0.6
Ho	LF200	0.02	0.3	0.7	0.1	0.3	0.1	0.2	0.1	0.9	0.1	0.1	0.2	0	0.2	0.1	0.3	0.1	0.1
Er	LF200	0.03	0.9	2.1	0.2	0.7	0.2	0.6	0.3	2.2	0.3	0.4	0.6	0.1	0.5	0.3	0.7	0.3	0.3
Tm	LF200	0.01	0.1	0.3	<0.01	0.1	0	0	0	0.3	0	0	0.1	<0.01	0.1	0	0.1	0	0
Yb	LF200	0.1	0.6	1.5	0.1	0.4	0.1	0.3	0.3	1.7	0.2	0.3	0.4	0.1	0.4	0.3	0.4	0.3	0.2
Lu	LF200	0.01	0.1	0.2	<0.01	0.1	0	0	0	0.2	0	0	0.1	<0.01	0	0	0.1	0	0
Mo	AQ200	0.1	4	5.5	2.6	9.8	1.4	3.4	5.7	9.2	1.1	5	1.1	2.3	3.1	9.6	3.8	2.5	0.8
Cu	AQ200	0.1	1.8	67.6	3.6	35.3	4.4	37.3	7.6	44.7	24.7	7.1	6.4	20.9	2.7	9.9	11.8	10.2	1.9

(*continued on next page*)

Table 4 (*continued*)

	Sample ID	MDL	JSMAR4	JSMAR5	JSMAR7	JSMAR8	JSMON H9	JSMON13	JSMON16	JSMON18	JSMON2	JSMON20	JSMON23	JSMON25	JSMON29	JSMON31	JSMON33	JSMON39	JSMON3b
Pb	AQ200	0.1	2011.8	>10000.0	5034.1	>10000.0	71.3	7553.9	>10000.0	>10000.0	8107	4610.3	74.7	>10000.0	483.9	2054.4	>10000.0	1303.9	24.2
Zn	AQ200	1	>10000	>10000	5765	>10000	192	>10000	>10000	>10000	>10000	>10000	>10000	>10000	>10000	>10000	>10000	6929	4675
Ni	AQ200	0.1	27	3.7	4.9	24.7	2.2	104.5	10.3	66.2	1.8	32.9	9	18.3	22	14.7	9.8	15.6	1.5
As	AQ200	0.5	3.9	1.6	8.9	3.3	0.7	1.1	19.2	24.5	0.6	17.2	2.8	30.3	1.4	28.8	4.3	17.3	1
Cd	AQ200	0.1	>2000.0	>2000.0	376.9	1490.7	4.8	>2000.0	69.3	33.4	440.7	152	10.4	588.9	439.7	42.4	59.6	6	57.2
Sb	AQ200	0.1	0.1	0.2	<0.1	<0.1	<0.1	<0.1	0.2	0.2	0.1	<0.1	<0.1	0.1	<0.1	0.5	0.4	0.1	<0.1
Bi	AQ200	0.1	<0.1	<0.1	<0.1	<0.1	<0.1	<0.1	<0.1	<0.1	<0.1	<0.1	<0.1	<0.1	<0.1	<0.1	<0.1	<0.1	<0.1
Ag	AQ200	0.1	55	7	2.5	4.8	0.2	19.1	11.6	36	24.3	4.4	35.5	4.8	4.6	3.7	41.4	0.2	1.4
Au	AQ200	0.5	<0.5	<0.5	<0.5	<0.5	<0.5	<0.5	0.8	2	<0.5	<0.5	<0.5	<0.5	<0.5	<0.5	<0.5	1.3	<0.5
Hg	AQ200	0.01	0.2	0.2	0.1	0.2	0	1.2	0.2	0.2	0.2	0.6	0.3	0.7	0.1	0.2	0.1	0.1	<0.01
Tl	AQ200	0.1	5.3	1.9	0.2	4.4	<0.1	3	0.2	1.8	1.1	0.5	1.1	1.4	2.7	1.3	0.2	0.3	<0.1
Se	AQ200	0.5	1	0.7	<0.5	3.2	<0.5	2.1	1.7	1.7	0.7	1.8	<0.5	<0.5	3.6	1.1	<0.5	1	<0.5

Notes: "-" no detected; * corrected for oxides wt%. MDL = minimum detection limit. Methods (Bureau Veritas Commodities Canada ltd., Vancouver, Canada): LF202 package, which includes LF200, TC000 (IR Combustion – total C and S), and AQ200: $Li_2B_4O_7/LiBO_2$ + aqua regia (AQ) digestion ICP-ES/MS; GC806 FeO by Titration; GC816 Zn by Titration; GC817 Pb by Titration.

sheet silicates (white micas and smectites) feature around 2200 nm, pixels with (2) values>2.0 were masked out from further processing, then the *2200D* index (Al-sheetsilicate abundance "*ASA*"; Laukamp 2022; further developed based on Sonntag et al., 2012) was applied to the remaining pixels:

$$2200D = \frac{R2143 + R2229}{R2206} = \frac{\text{B125} + \text{B136}}{\text{B133}} \quad (3)$$

Pixels with (3) resulting values>2.15 were masked out to better delineate the areas effectively characterized by the presence of dolomites using the ratio *2320D/2350D* and evaluating compositional variation within dolomites.

The identification of the outcropping rocks dominated by Fe-oxyhydroxides (i.e., gossans) and nonsulfides, instead, was obtained through the *900D* relative depth index (Fe-(oxyhydr-) oxides abundance "*FOA*"; Laukamp 2022):

$$900D = \frac{R770 + R962}{R908} = \frac{\text{B44} + \text{B62}}{\text{B57}} \quad (4)$$

A rainbow color scale was applied to all the mineral maps, where red indicates higher abundances and blue indicates lower abundances referring to the upper and lower stretching limits reported in Table 2. This also allows a quick comparison with the binary discrimination diagrams. To obtain the hyperspectral mineral mapping performance assessment, *ROIs* were created on the L2C PRISMA VNIR-SWIR image over the areas where the target lithology (i.e., dolomite, limestone, gossan) was recognized by the PRISMA-derived mineral mapping. Statistics were extracted from each *ROI* and then directly compared to the field-based spectra representative of each target phase resampled to the PRISMA hyperspectral resolution (as explained in sub-section 4.1), after continuum removal to normalize the spectra.

5. Results

5.1. Quantitative mineralogy (XRPD-QPA), geochemistry, and absorption properties at PRISMA spectral resolution of ground samples

The three main groups of analyzed samples: host rock, gossans, and Zn- ore samples, were characterized by distinct features when comparing their mineralogy (Table 3), geochemistry (Table 4) and reflectance spectra properties (Figs. 5–7; Table 5).

Host rock samples. The group comprises five samples characterized by dolomite and calcite as main phases, and minor alteration minerals and impurities, such as smithsonite, goethite, smectite and kaolinite (Fig. 5 and Tab 3). The chemical composition of host rock limestones is defined by CaO contents of 54.73 wt% and very low MgO (0.25 wt%) (Table 4). SiO_2, Al_2O_3, Na_2O, K_2O, and MnO contents are always lower than 0.6 wt %. Dolomite-dominated samples are characterized by CaO values ranging between 30.04 wt% and 26.14 wt%, while MgO contents vary between 18.59 wt% and 15.14 wt% (Table 4). Fe_2O_3 values range between 0.5 wt% and 3.64 wt%. JSMON3b is the only sample characterized by significant content of bivalent iron (FeO of 1.89 wt%; Table 4). Except for Cd, which is higher for sample and JSMON2 compared to the other samples, and Ba, which reaches hundreds of mg/kg only in samples JSMON23 and JSMON H9, trace elements do not vary considerably for all the host rock samples and are generally negligible (Table 4).

Spectral signatures of limestones outcropping within the study area show a very pronounced CO_3-related absorption feature in the SWIR region at 2338 (limestone sample JSMON H9), with weaker features occurring at 2160 and 1755 nm (Fig. 5). The main CO_3 absorption feature, instead, appears shifted to shorter wavelengths in the dolomite spectra, with the main features occurring as variably deep absorptions around 2320 nm (Fig. 5). However, the same feature frequently appears shifted to longer wavelengths (between 2322 nm and 2324 nm) in almost all the samples, except for sample JSMAR4 (2320 nm). The left-hand asymmetry of the main CO_3 absorption feature, showing a

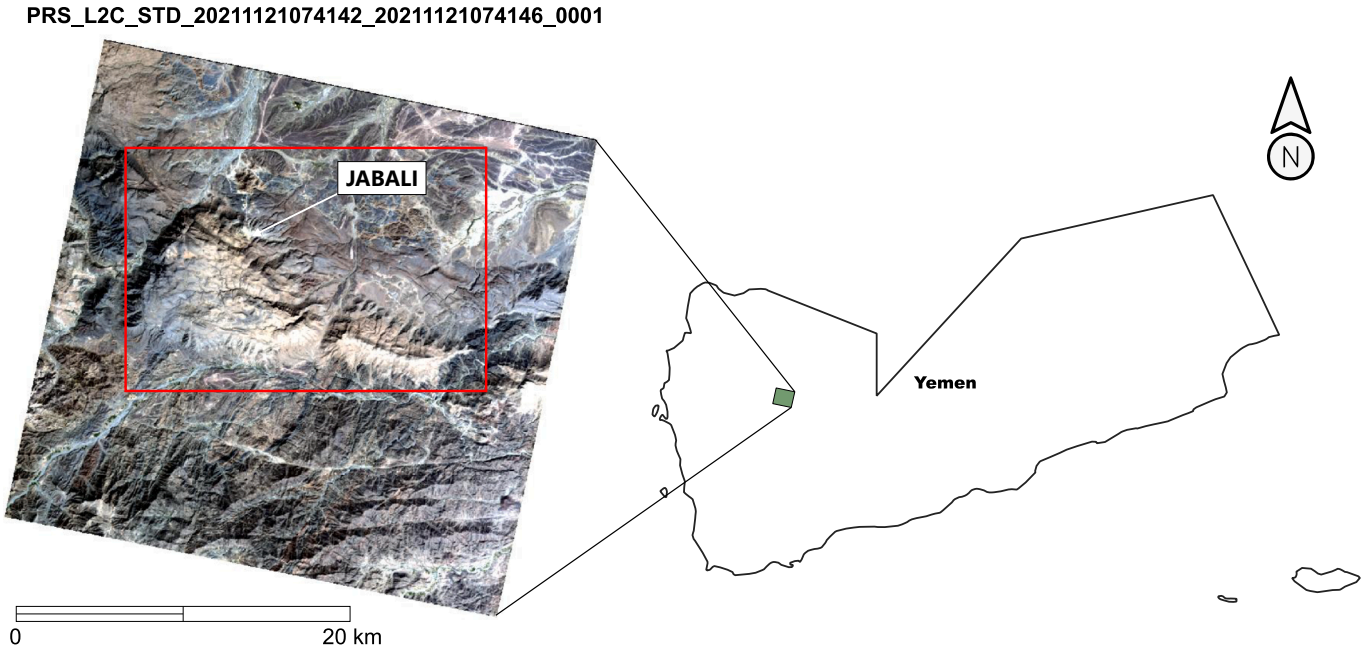

Fig. 3. The Jabali study area. PRISMA True colors image (product identifier: PRS_L2C_STD_20211121074142_20211121074146_0001) and its location. The red box highlights the processed Area of Interest subset. (For interpretation of the references to color in this figure legend, the reader is referred to the web version of this article.)

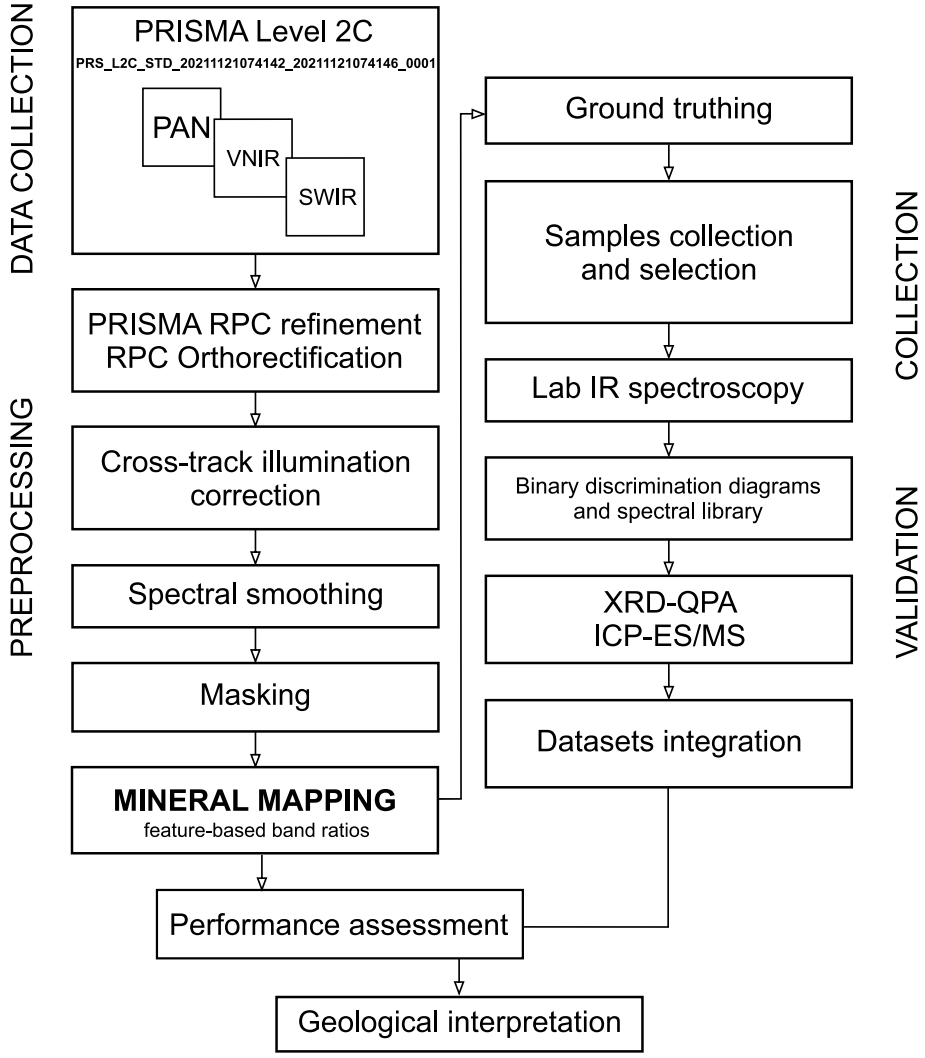

Fig. 4. Schematic multi-scale workflow used in this study.

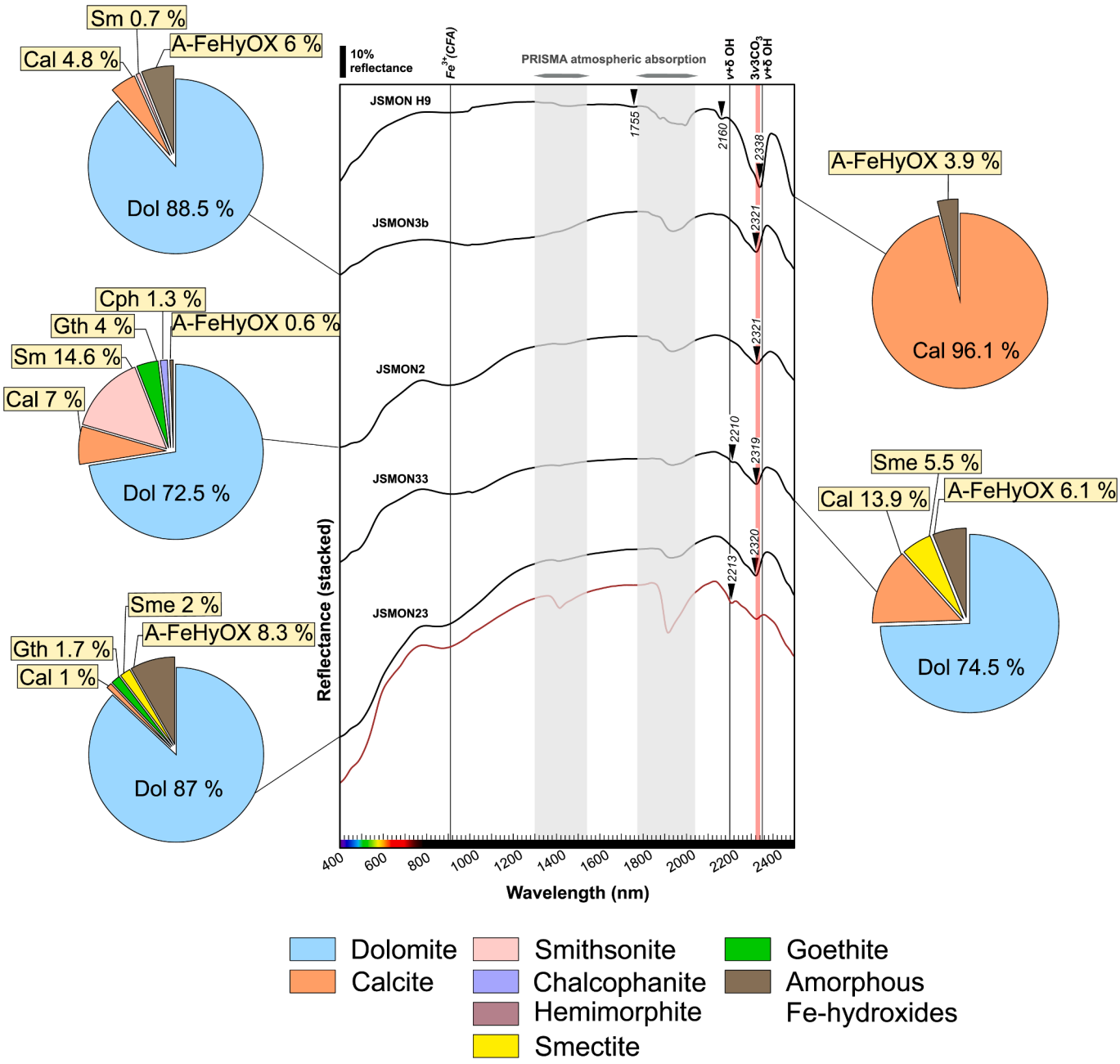

Fig. 5. Laboratory reflectance spectra downsampled to the PRISMA resolution in the VNIR-SWIR region, showing the spectral signatures for limestones and dolomites. For sample JSMON23 in red is shown the spectra acquired on the sample's weathered side. Pie charts showing the modal mineralogy of bulk samples obtained by XRPD-QPA are also shown for direct comparison. PRISMA spectral bands strongly affected by atmospheric absorption are marked at the top of the diagram and were excluded from mineral mapping processing. Abbreviations explanation in Table 3. (For interpretation of the references to color in this figure legend, the reader is referred to the web version of this article.)

shoulder on the short-wavelength side, is ubiquitously present in all the carbonate-bearing samples. Sample JSMON33 and the more weathered side of sample JSMON23 show the Al-OH feature at around 2210 nm, in the latter sample accompanied by a deepening in the water and hydroxyl-related feature (1416 nm and 1914 nm) (Fig. 5). The broad Fe-related absorption feature in the VNIR region for the dolomite-dominated samples, centered in the range from 900 nm to 950 nm, may be associated with goethite (when present) and/or Zn-Fe-bearing altered dolomites (CFA). An exception is the unaltered portion of sample JSMON3b, characterized by a shallower, but broader, absorption centered around 1000 nm to 1200 nm (a broad absorption doublet is more visible in continuum removed spectrum) due to Fe^{2+} contribution. Smectite (Zn-bearing smectite sauconite) occurring in sample JSMON33 (5.5 wt% from XRPD-QPA analysis) is visible at 2210 nm (Zn-OH and/or Al-OH feature) (Fig. 5). The contribution of water and hydroxyl-bearing material is ubiquitously represented by two variably deep absorption features close to 1900 nm and 1400 nm, which may, in some cases, appear shifted due to the occurrence of specific hydrous phases (Table 5).

Gossan samples. In these heterogeneous samples goethite ubiquitously predominates, followed by calcite with lesser amounts of hematite (Fig. 6). Quartz, K-Fe-Pb-bearing sulfates (jarosite and plumbojarosite) and kaolinite, gypsum, and Zn-bearing smectite were also observed in lower amounts (Fig. 6 and Table 3), except for sample JSMON18, where plumbojarosite occurs up to 16.5 wt% and Zn-bearing smectite shows amounts of 8 wt%. The specimens from the gossan are

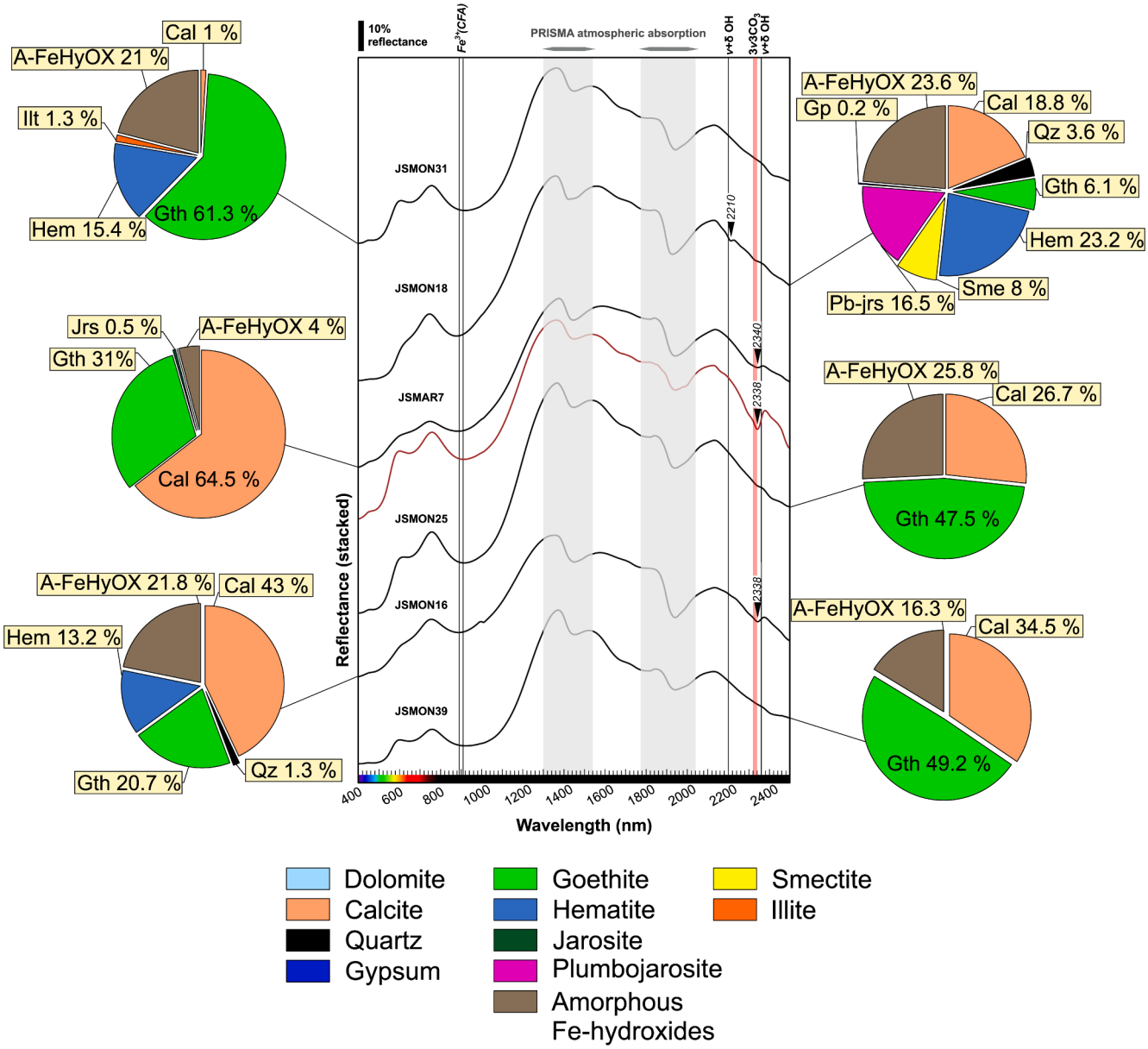

Fig. 6. Laboratory reflectance spectra downsampled to the PRISMA resolution in the VNIR-SWIR region, showing the spectral signatures for gossan samples. For sample JSMAR7 in red is shown the spectra acquired on the sample's weathered side. Pie charts showing the modal mineralogy of bulk samples obtained by XRPD-QPA are also shown for direct comparison. PRISMA spectral bands strongly affected by atmospheric absorption are marked at the top of the diagram and were excluded from mineral mapping processing. Abbreviations explanation in Table 3. (For interpretation of the references to color in this figure legend, the reader is referred to the web version of this article.)

marked by very high bulk Fe_2O_3 contents ranging from 78.9 wt% to 28.2 wt% (Table 4). SiO_2 values are generally between 2 and 3 wt%, except for sample JSMON18 (8.08 wt%), which is also characterized by significant Al_2O_3 values of about 4.5 wt% (Table 4). Calcite-bearing gossan samples are characterized by CaO values varying between 10.59 wt% and 36.04 wt% (Fig. 6; Table 3 and 4), with mean values of about 20 wt%. MgO contents are ubiquitously very low, showing mean values of 0.28 wt%, and always below 0.3 wt%. Variable ZnO contents were observed between 0.6 wt% and 3.7 wt%. PbO is generally low; contents of 6 wt% are shown by sample JSMON18, followed by sample JSMON16, which is characterized by PbO values of 3.23 wt% (mean values of about 2 wt%). The other gossan samples have very low PbO values (Table 4). Most variable trace elements observed in the samples from gossan zones are Cd, Cu, Ag, Ni, Cu, V, Ga, Co (Table 4). However, bulk concentrations reaching hundreds of mg/kg were only observed for Cd (mean 482 mg/kg Cd) in samples JSMAR7 and JSMON25, while it is always lower than about 70 mg/kg for all the other samples belonging to this group (Table 4).

The gossan samples dominated by goethite show the main absorption features at 660 nm (CFT) and 908 nm – 920 nm (CFA), except for sample JSMON18, where the CFA is slightly shifted to shorter wavelengths (878 nm) due to greater hematite content (Fig. 6). The CO_3 main feature occurs generally at around 2338 nm, but it is ubiquitously very weak due to the low calcite content, except for sample JSMAR7 and sample JSMON16, where calcite concentration is higher (Cal 64.5 wt%, and 43 wt%). Sample JSMON18, instead, is characterized by the presence of the Al-OH feature at 2210 nm (Fig. 6) due to the higher presence either of plumbojarosite (16.5 wt%) and smectites (Sme 8 wt%).

Zn ore samples. In these samples, hydrozincite is the most abundant mineral, followed by hemimorphite, with lesser smithsonite (Fig. 7 and Table 3). Goethite occurs in higher quantities in sample JSMON20 (40.4 wt%). The sample JSMON13, instead, is characterized predominantly by

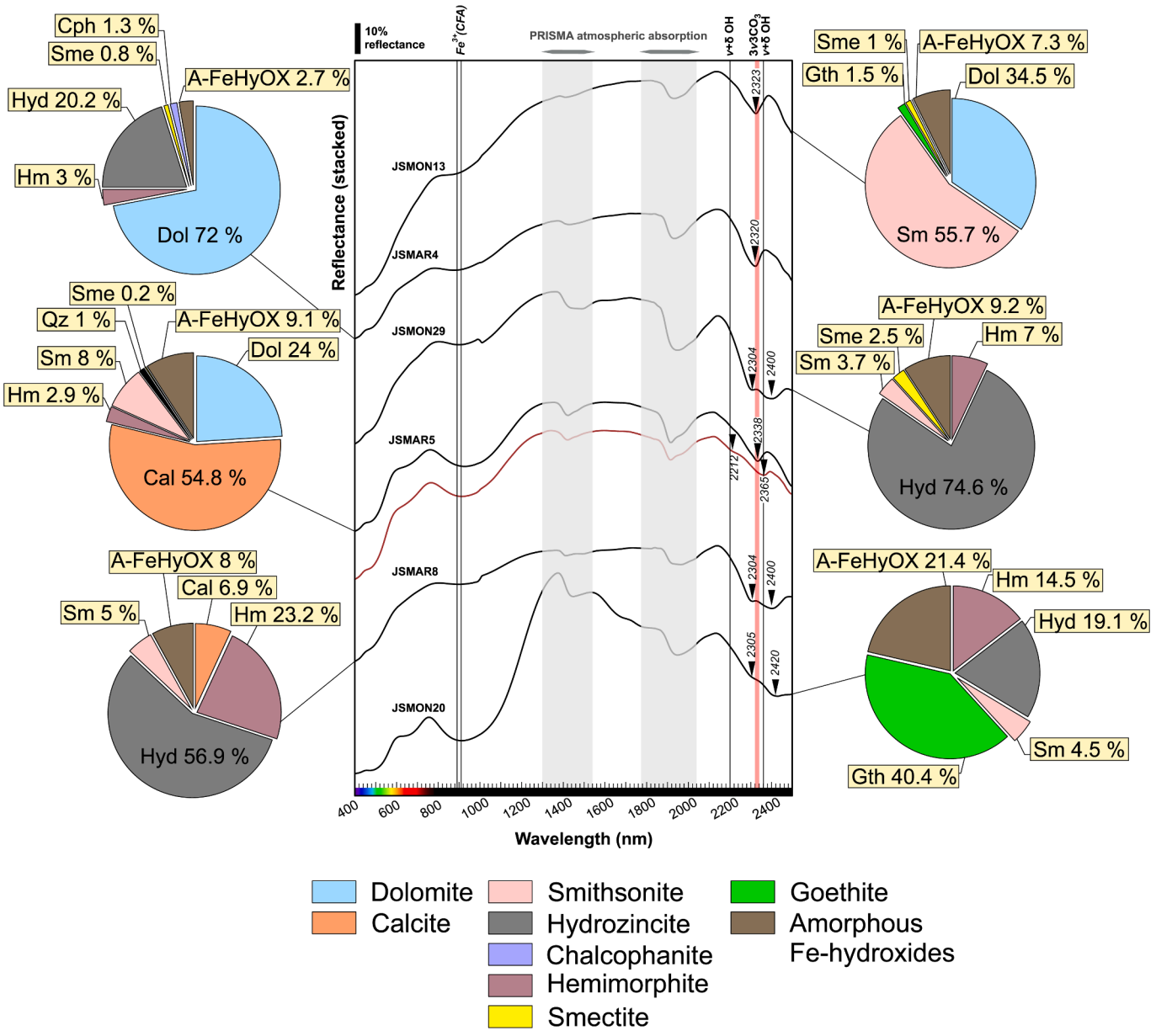

Fig. 7. Laboratory reflectance spectra downsampled to the PRISMA resolution in the VNIR-SWIR region, showing the spectral signatures for Zn ore samples. For sample JSMAR5 in red is shown the spectra acquired on the sample's weathered side. Pie charts showing the modal mineralogy of bulk samples obtained by XRPD-QPA are also shown for direct comparison. PRISMA spectral bands strongly affected by atmospheric absorption are marked at the top of the diagram and were excluded from mineral mapping processing. Abbreviations explanation in Table 3.

smithsonite (55.7 wt%) and dolomite (34.5 wt%), with goethite (1.5 wt %) as a minor phase, and smectite in traces (1 wt%) (Fig. 7 and Table 3). Zn ore samples are characterized by bulk MgO and CaO concentrations up to 14.9 wt% and 37.3 wt%, respectively. SiO_2 is generally equal or slightly lower than 2 wt%, except for sample JSMON20, defined by bulk SiO_2 contents of 4.4 wt%. ZnO concentrations are always higher than 20 wt%, reaching bulk contents of 65.7 wt% (Table 4). PbO contents are generally very low and never higher than 0.81 wt%. Fe_2O_3 bulk contents observed are between 2.3 wt% and 6.54 wt% (mean values of 5.2 wt%), aside from sample JSMON20 (Fe_2O_3 of 50.9 wt%) (Table 4). Bulk Cd concentrations are high for all the samples belonging to this group (Table 4), showing values above the detection limit (2000 mg/kg) for the smithsonite and hydrozincite-bearing samples.

The smithsonite-hydrozincite bearing samples are characterized by a broad absorption doublet at 2304 and 2400 nm (Table 3; Fig. 7), resulting from the overlapping of the CO_3 features of the two Zn-bearing carbonates, not allowing their clear distinction in any of the investigated samples. A very weak band at 2210 nm characterizes the altered portion (red spectrum in Figure 7) of sample JSMAR5, which may be associated with the Zn-OH bond in hemimorphite (Figure 7). A deep and broad absorption centered around 920 nm, instead, may be related to the presence of either Fe-hydroxides or Fe impurities. However, the sample JSMON20, characterized by goethite as the main phase (40.4 wt%), clearly shows the typical CFT and CFA features at 670 nm and 912 nm, respectively. The sample JSMON13, instead, is characterized by a smithsonite-dolomite ratio close to 1:1, it is only defined by a "rather" symmetric absorption band centered at 2323 nm (Fig. 7).

5.2. *Relationships between spectral properties and ICP-MS/ES geochemical data of ground samples*

The same feature extraction indices applied to the PRISMA L2C scene

Table 5
Mineral assemblage (in abundance order from XRPD-QPA analysis) and VNIR-to-SWIR continuum-removed spectral feature positions in nm. When differences occurred in a sample, both fresh and weathered sides were acquired. Abbreviations are explained in Table 3.

Sample ID	Mineral Assemblage	Acquired portion	Characteristic spectral features in VNIR (nm)	Characteristic spectral features in SWIR (nm)
JSMON2	Dol + Cal + Sm + Gth + Cph + A-FeHyOX	fresh side	950	1438 (weak), 1935, 2322
		weathered side	918	1430 (very weak), 1941, 2322
JSMON3b	Dol + Cal + Sm (tr.) + A-FeHyOX	fresh side		1050, 1270, 1414 (very weak), 1938, 2320
		weathered side	940	1298 (very weak), 1414 (weak), 1940, 2320
JSMAR4	Dol + Hz + Hm + A-FeHyOX	fresh side	945	1425, 1934, 2315
		weathered side	950	1429, 1931, 2296, 2392
JSMAR5	Cal + Dol + A-FeHyOX	fresh side	673 (weak), 970	1425, 1916, 2334
		weathered side	673 (weak), 970	1425, 1916, 2210 (very weak), 2350
JSMAR7	Cal + Gth + Jrs + A-FeHyOX	fresh side	676, 940	1440, 1940, 2303, 2334
		weathered side	670 (weak), 970	1442, 1939, 1670, 1770, 1937, 2337
JSMAR8	Hyd + Hm + Cal + A-FeHyOX		970	1405, 1967, 2300, 2375
JSMON H9	Cal + A-FeHyOX			1415, 1876–1995, 1755, 2158, 2338
JSMON13	Sm + Dol + Gth + A-FeHyOX		942	1434 (very weak), 1937, 2320
JSMON16	Cal + Gth + Hem + A-FeHyOX		667 (weak), 925	1443, 1762 (very weak), 1938, 2216 (extremely weak), 2339
JSMON18	Cal + Hem + Pb-Jrs + A-FeHyOX		670, 908	1416, 1924, 1672 (very weak), 1780 (weak), 1925, 2208, 2325
JSMON20	Gth + A-FeHyOX		670, 980	1437, 1680, 1778, 1941, 2300, 2401
JSMON23	Dol + A-FeHyOX	fresh side	916	1416 (very weak), 1938, 2320
		weathered side	680 (very weak), 916	1416, 1916, 2208, 2255, 2319
JSMON25	Gth + Cal + A-FeHyOX		668, 970	1437, 1940, 1675 (very weak), 1776, 1931, 2333 (very weak), 2405 (very weak)
JSMON29	Hyd + A-FeHyOX		962	1490, 1940, 2299, 2371
JSMON31	Gth + Hem + A-FeHyOX	fresh side	672, 963	1442, 1937, 1670, 1775 (weak), 2268 (extremely weak), 2410 (weak)
		weathered side	672, 963	1442, 1937, 1670, 1775 (weak), 2268 (extremely weak), 2410 (weak)
JSMON33	Dol + Cal + A-FeHyOX	fresh side	965	1414 (extremely weak), 1938, 2209, 2320
		weathered side	966	1438 (weak), 1937, 2322
JSMON39	Gth + Cal + A-FeHyOX		678, 1010	1443, 1941, 1680, 1777, 1936, 2335 (extremely weak), 2404

were also used for describing the spectral behavior of the ground samples and colored using the variable in y-axes, to improve the comparison with the mineral maps (Fig. 8 a-f). The same indices were plotted against MgO, CaO, and Fe_2O_3 bulk concentrations and shown in Fig. 9 a-d. The *2350D* was plotted against the Carbonate Composition script to characterize the occurrence and the compositional variations between the carbonate phases (Fig. 8a). The deeper relative depth of the spectral feature at around 2340 nm in calcite-bearing samples resulted in higher *2350D* values (orange to red samples dots), while the dolomites form a cluster defined by lower values compared to limestones (blue samples dots). A threshold value of 2.0 is observed. The *2320D* feature extraction script was used to better define the dolomites samples (diagnostic feature centered between 2322 nm and 2324 nm) and correctly evaluate their abundances. The dolomite-bearing samples place above the *2320D* threshold value of 2.02, directly proportional to the dolomite content in the studied samples (green to red samples points in Fig. 8b).

Lower *2320D* values (2.04) are observed for sample JSMON13, characterized by 34.5 wt% dolomite, while higher *2320D* values are shown by sample JSMON3b (Dol 88.5 wt%). A positive correlation ($y = 186.85x - 374.62$, $R^2 = 0.84$) is noticed for the bulk MgO (wt%) concentration. Dolomite samples show both higher *2320D* and MgO (wt%) values (Fig. 9a). The *2350D* and *2320D* feature extraction scripts were plotted against each other (Fig. 8C) as they are negatively correlated. The binary discrimination diagram is colored by the ratio *2320D/2350D*, which highlights the two resulting trends. The latter trends are indicated by arrows in Fig. 8c, discriminating both dolomites (green to red samples points in Fig. 8c, indicating higher *2320D* and lower *2350D*) and limestones (blues samples points in Fig. 8c; defined by lower *2320D* and higher *2350D*) and their increasing abundance. A very good correlation is shown by plotting the *2320D/2350D* ratio values and the MgO (wt%) bulk concentrations in host rock samples ($y = 138.25x - 133.59$, $R^2 = 0.86$) (Fig. 9c). Two defined trends, instead, can be noticed by plotting the ratio against the CaO (wt%), where calcite-bearing samples place at high CaO (wt%) values and low *2320D/2350D* (Fig. 9c). The gossan samples, instead, were analyzed through the *900D* feature extraction script, plotted against the Hematite-Goethite ratio, to define their abundance in the analyzed samples and composition (predominance of either goethite or hematite in the samples), respectively (Fig. 8d). Gossan samples are defined by higher *900D* values, shown by the green to red dots in Fig. 8d, placing above the threshold value of around 2.3. Goethite-dominated samples (diagnostic CFA absorption feature occurring between 905 nm and 909 nm) show an increase of the *900D* values directly correlated with the goethite abundances obtained through XRPD-QPA analyses. Sample JSMON 31 (61.3 wt% Gth) is characterized by *900D* values at around 2.8, while *900D* close to 2.44 defines sample JSMAR7 (31 wt% Gth) (Fig. 8d). A shift to shorter

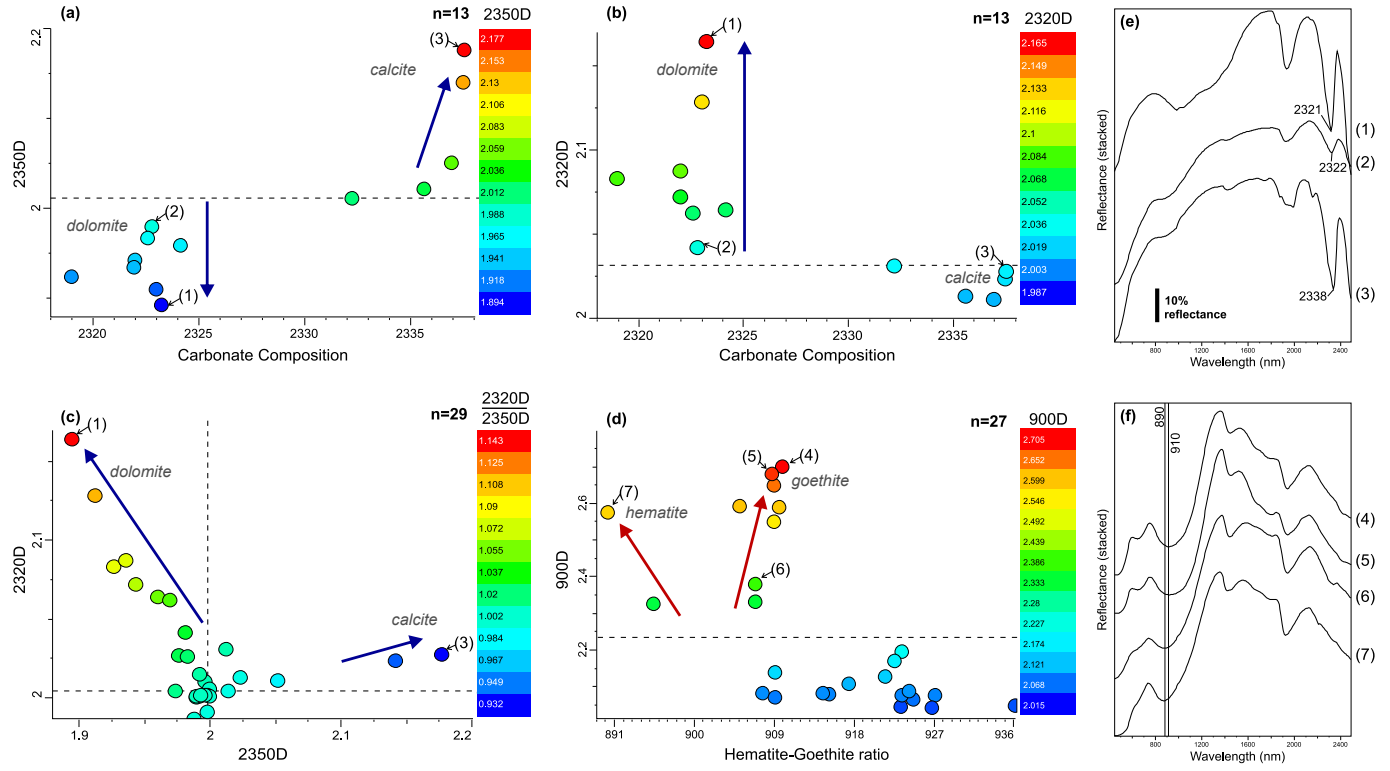

Fig. 8. Binary discrimination plots for the ground samples reflectance spectra dataset. (a) *2350D* versus Carbonate Composition colored following the *2350D*. Dolomite samples in blue are characterized by *2350D* values lower than 2.0, while values above 2.20 are shown by limestones samples (orange-to-red). In green colors are shown the rusty and partially dedolomitized dolomite samples and the calcite-bearing gossan sample. (b) *2320D* versus Carbonate Composition colored following the *2320D*. The dolomite-bearing samples are shown as green to red samples points and placed above the *2320D* threshold value of 2.02. Calcite-bearing samples plotted as light blue dots are characterized by *2320D* lower than 2.02. (c) *2350D* versus *2320D* diagram, colored following the *2320D/2350D* ratio. Dolomites samples (green to red dots) and limestones (blue dots) are negatively correlated, the distribution trends are indicated by the arrows. (d) *900D* plotted against Hematite-Goethite ratio. Gossan samples are characterized by values higher than 2.3. (e) spectra of representative host rock samples, (1) and (2) indicate decreasing dolomite content; (3) refers to limestone sample. (f) spectra of representative gossan samples order as decreasing goethite content (4, 5, 6) and hematite (7). The numbers refer to their position in the binary diagrams. Arrows indicate increasing mineral abundances. (For interpretation of the references to color in this figure legend, the reader is referred to the web version of this article.)

wavelengths is observed for hematite-bearing samples, proportional to increasing hematite abundances (23.2 wt% and 13.2 wt%, respectively). As shown before for host rock samples, also the Fe_2O_3 (wt%) bulk content for the analyzed samples is highly correlated with the *900D* index ($y = 96.756x - 196.58$, $R^2 = 0.93$) (Fig. 9d). In particular, the highest Fe_2O_3 (wt%) values were measured for goethite-dominated samples, which are also characterized by high *900D* values.

5.3. Mineral maps obtained through hyperspectral satellite remote sensing

In Fig. 10a-c, and 11a, the band depth indices proposed in this study, *2350D, 2320D, 2200D,* and *900D* are shown. In the *2350D* mineral map (Fig. 10a), the distribution of dolomites and volcanic rocks outcropping in the study area is shown in blue, indicated by pixels values below the observed 2.0 threshold. Limestones are highlighted in red colors. In Fig. 10b, the *2320D/2350D* ratio map shows in red the pixels that are defined by a strong 2320 nm feature depth, allowing a clear definition of the dolostones distribution within the study area, while limestones are characterized by lower values (shown in blue Fig. 10b). The 2200 nm feature depth map 2200D is shown in Fig. 10c. The areas characterized by higher and lower relative abundances of Al-sheet silicates (micas) are highlighted in red (higher) and blue (lower). The *900D* mineral map (Fig. 11a and b) shows in red the Fe^{3+}-bearing rocks, characterized by higher *900D* values (Fig. 11a). The group includes the gossans outcrops, but also red beds and granite complexes. As the latter lithologies were identified also in the *2200D* map, they could be excluded from further interpretation. The known gossan distribution was highlighted, together with possibly new identified gossans a few kilometers E-NE from the Jabali prospect area (Fig. 11b).

5.4. Comparison between PRISMA L2C results and field-based hyperspectral data

The spectra derived from the selected ROIs created on the PRISMA L2C VNIR-SWIR scene over the areas recognized as (a) dolomites (Fig. 10b), (b) limestones (Fig. 10a) and (c) gossans (Fig. 11a) are reported in Fig. 12a–c. In detail, Fig. 12a–c shows the comparison between some representative field-based spectra downsampled to the PRISMA spectral resolution, and the spectra derived from the defined ROIs over the PRISMA image (black dotted lines). The intervals chosen are SWIR-2 (2200–2400 nm) and VNIR (400–1000 nm). The spectral signatures generally appear consistent with those obtained from laboratory hyperspectral measurements. The differences visible may be due to PRISMA 30 m-spatial resolution and mineral phases mixing compared to the spectra collected under laboratory conditions. However, a slight shift towards longer wavelengths (of about 7 nm) can be noted between the limestone spectrum (JSMON H9) and the PRISMA selected ROIs spectrum. The dolomite absorption feature, instead, is visible at 2320 nm in both the PRISMA spectra and the dolomite samples spectra. Regarding the gossan samples, Fe-hydroxides spectral features (CTF and CFA) are quite well visible, despite some distortions, due perhaps to non-absorption and absorption bands applied in the L2 processing for water columnar content assessment. Fig. 12d, instead, shows the same spectra in Fig. 12a–c after applying the *2350D* and the *2320D* band ratios, then

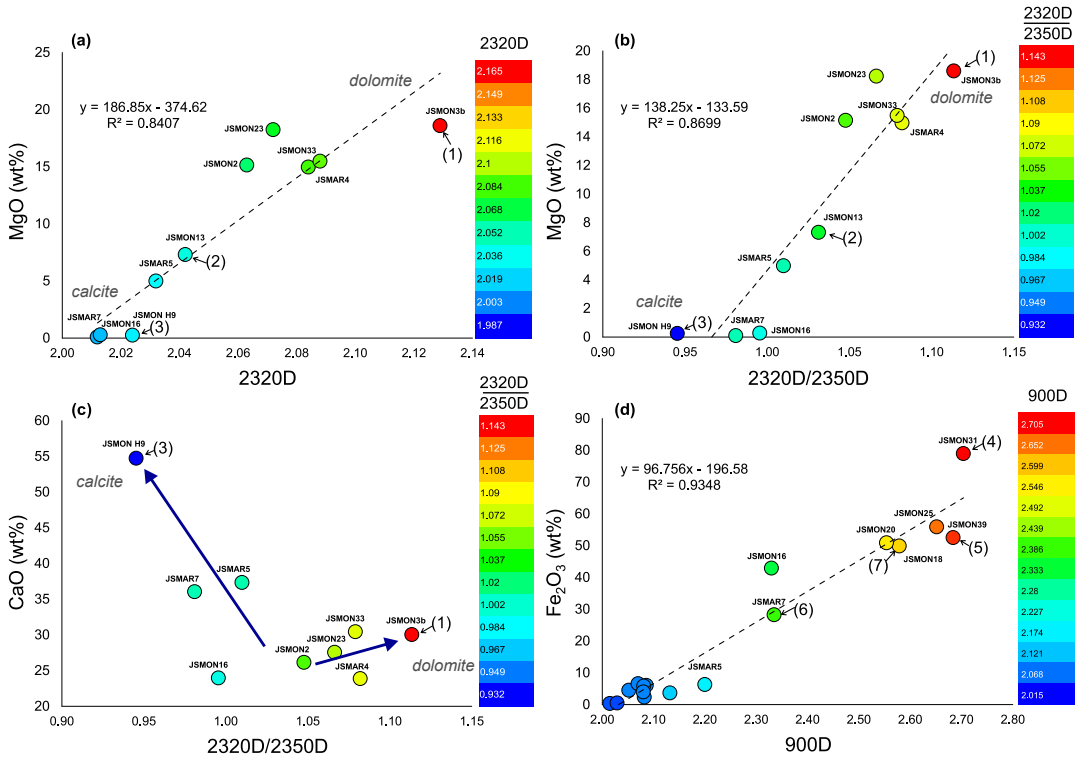

Fig. 9. Validation Binary plots reporting the integration with whole-rock geochemical data; (a) *2320D* plotted versus MgO (wt%), colored following *2320D*; (b) *2320D/2350D* ratio plotted versus MgO (wt%), colored following *2320D/2350D*; (c) *2320D/2350D* ratio plotted versus CaO (wt%), colored following *2320D/2350D*; (d) *900D* plotted versus Fe_2O_3 (wt%), colored following *900D*.

plotted against each other and colored following the *2320D/2350D* ratio in order to facilitate the comparison with the binary discrimination plots (see sub-section 4.2) and the mineral maps (see sub-section 4.3). As shown by the binary plot, the spectra derived from the PRISMA selected ROIs fall into the respective group (either dolomites or limestones), in agreement with the field-based hyperspectral data chosen for validation.

6. Discussion

6.1. Dolomite identification and mapping

Due to their spectral contrast, the distribution of the main rock types outcropping in the Sab'atain basin, such as limestone, dolomite, Precambrian basement granites, and Tertiary volcanism products can be mapped using the workflow proposed in this study (Fig. 13a, b; see the simplified geological map for comparison Fig. 1b). In addition, by comparing the obtained PRISMA-derived spectral maps with the geological field data shown in previous studies (e.g., Christmann et al., 1989; Al Ganad et al., 1994 and references therein), it is shown that PRISMA data also allows delineation of the alteration at regional scale, providing information about prospective zones for mineral exploration.

Distinction between dolomites and limestones was possible based on the main CO_3^{2-} absorption feature, which appears shifted to shorter wavelengths for dolomites, with the main feature occurring at 2320 nm (Gaffey 1986; Lampinen et al., 2019), compared to the main calcite absorption feature located at 2335 to 2340 nm (Clark et al., 1990; Van der Meer 1995; Kurz et al., 2012). Dolomite-dominated samples used for validation of the Jabali deposit area are characterized by dolomite abundances ranging from ~ 73 to 88 wt% (Fig. 5, samples JSMON3b, JSMON2, JSMON33, and JSMON23). Reflectance spectra from FieldSpec data show that most of them cluster between 2322 nm and 2324 nm (Fig. 5, 8a–c), shifted to longer wavelengths compared to the diagnostic wavelength position of stoichiometric dolomite at around 2320 nm, except for sample JSMAR4. When comparing both *2320D* and *2350D* feature extraction indices with XRPD-QPA analyses, it appears that dolomite-dominated samples are characterized by an increase of the *2320D* values, directly correlated with the dolomite abundances gained through XRPD-QPA analyses, while they are inversely correlated with *2350D* values, which decrease with increasing dolomite abundances. On the contrary, calcite-bearing samples (both limestones and alteration samples) show an increase of the *2350D* proportional to the XRPD-QPA calcite abundances (Fig. 5, 8a–c). When comparing the *2320D* and *2350D* feature extraction indices with the whole-rock geochemical analyses, a positive correlation ($y = 186.85x - 374.62$, $R^2 = 0.84$) is shown between the bulk MgO (wt%) concentration and the *2320D* index, which is higher for samples with high MgO (wt%) values (Fig. 9a). A very high correlation ($y = 138.25x - 133.59$, $R^2 = 0.86$) was also obtained by comparing the *2320D/2350D* ratio with the MgO (wt%) bulk concentrations in host rock samples. Moreover, two defined trends can be noticed by correlating the *2320D/2350D* ratio against the CaO (wt%), where calcite-bearing samples (JSMON H9 and, secondly, JSMAR7 and JSMAR5) show high CaO (wt%) values and low *2320D/2350D* (Fig. 9c). These relationships demonstrate the value of the *2320D* and *2350D* feature extraction indices for the discrimination of limestone from dolomite.

As in several carbonate-hosted Zn-Pb deposits (e.g., Poland, USA, Ireland; Leach et al., 2005; Davies and Smith 2006), the hydrothermal dolomite at Jabali is Fe- and Mn-bearing (containing up to 2 wt% MnO and between 0.1 and 6 wt% FeO). As outlined in previous studies (Gaffey 1985, 1986; Kurz et al., 2012; Green and Schodlok 2016; Lampinen et al., 2019), higher Mn and Fe contents can cause the shift to longer wavelengths of the main carbonate bands in dolomite spectra, however, a discriminator between Fe-carbonate species is the Fe^{2+} CFA feature, a broad double band in the NIR region centered at around 1200 nm. From hyperspectral analysis from hand specimens, the latter aspect is visible only in the slightly Fe-enriched dolomite in sample JSMON3b for which, together with the presence of a broad but weak absorption doublet around 1200 nm (Figs. 5, 8e and Table 5), the bulk FeO contents

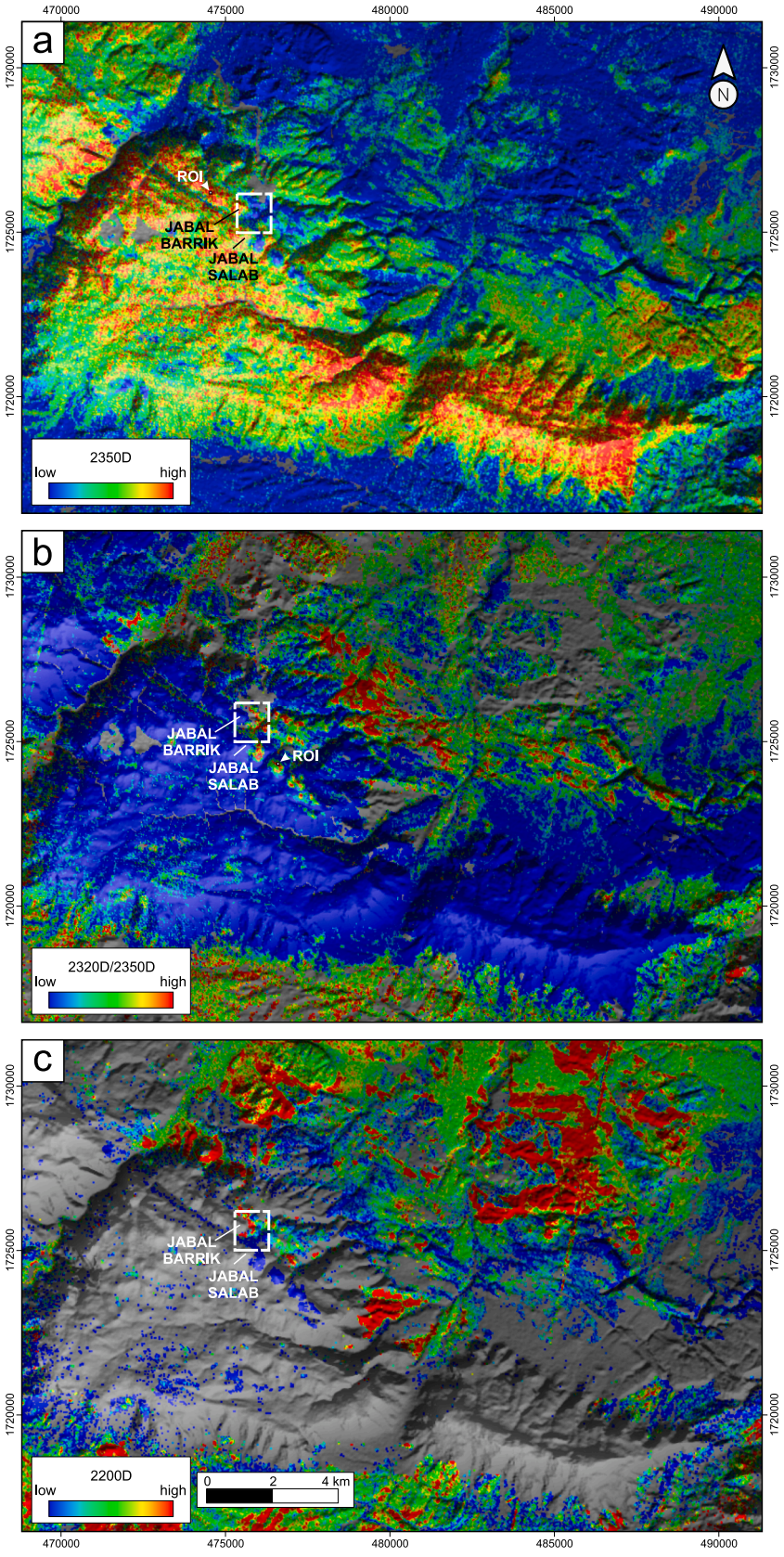

Fig. 10. Relative absorption depth indices applied to the PRISMA L2C scene of the Jabali area: (a) 2350 nm feature depth (*2350D*) map masked for vegetation and man-made features; (b) *2320D/2350D* ratio masked for *2200D* > 2.15. (C) 2200 nm feature depth (*2200D*) masked for *2350D* > 2.0, vegetation, and man-made features; Topographic shaded relief from SRTM NASA Version 3 data (Farr et al. 2007; NASA JPL, 2013) is used as background. The borders of Fig. 2 are reported as white dotted squares for localizing the Jabali area.

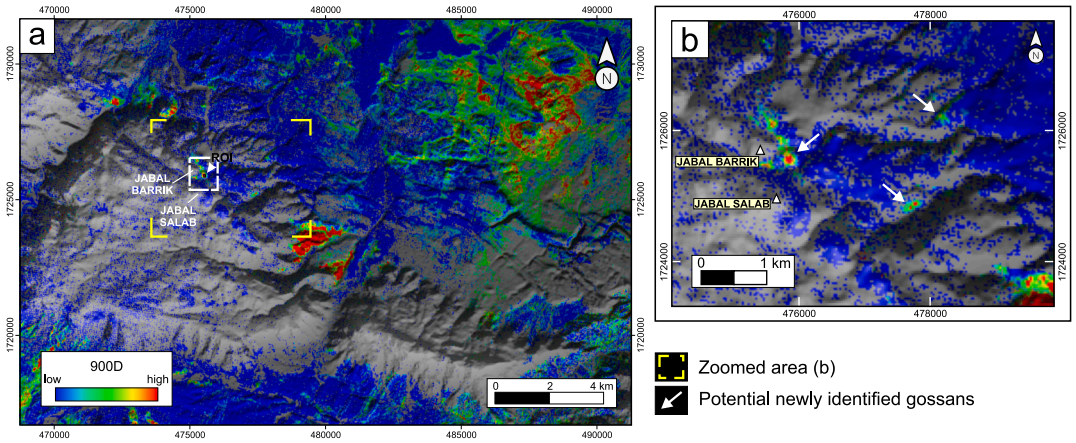

Fig. 11. (a) Ferric Oxides Abundance (*900D*) map and (b) a focus on the Main Area Of Interest. Topographic shaded relief from SRTM NASA Version 3 data (Farr et al. 2007; NASA JPL, 2013) is used as background. The borders of Fig. 2 are reported as white dotted squares for localizing the Jabali area.

obtained from whole-rock geochemical analysis show values up to ~ 1.9 wt% (Table 4). Samples JSMON2, JSMON33, and JSMON23, instead, show FeO concentration always lower than the detection limits (i.e., FeO < 0.20 wt%; Table 4) and are less pure, characterized by typical alteration products such as smithsonite and chalcophanite (JSMON2), goethite (JSMON2 and JSMON23) and smectites (i.e., sauconite; JSON33 and JSMON23; Fig. 5 and Table 5). At the same time, the latter samples show a broad absorption feature in the VNIR region at shorter wavelengths compared to ferroan hydrothermal dolomites (sample JSMON3b), centered from around 910 nm up to 940 nm (Fig. 5 and Table 5). The presence of this feature could be mostly related to the presence of goethite and/or amorphous Fe-hydroxides, which are characterized by the CFA feature occurring at around 908 nm (Crowley et al., 2003). However, the hydrothermal dolomite at Jabali also experienced later supergene alteration and formation of Zn-bearing dolomite (Mondillo et al., 2014), associated with the oxidation of Zn-Pb sulfide ores (Boni et al., 2011). Thus, the goethite-related absorption (Fe^{3+} CFA) in the dolomite samples could have been affected by a shift to longer wavelengths, potentially related to the presence of Zn^{2+}, similarly to smithsonite which displays deep and broad crystal field effects between 800 nm and 1200 nm and centered around 960 nm (McConachy et al., 2007).

Regarding the satellite spectral mapping, dolomite feature-based distribution maps of the Jabali deposit area could be obtained from the successive application of the latter tested indices targeting the relative depths and wavelength positions of the carbonate phases absorptions. The *2320D* index and its relationship with the *2350D* index applied to the PRISMA L2C scene allow the discrimination of dolomites from calcite-bearing outcrops/samples (Fig. 8a–c, Fig. 9a–c, Fig. 10a, b). In the *2320D/2350D* mineral map (Fig. 10b), limestones were highlighted in blue, and different dolomite types are characterized by shades of red (high relative abundances) to green (lower relative abundances). The spectra derived from selected ROIs (Fig. 12a, b, and d) confirm and validate the accuracy of the mineral mapping.

The application of the 2200D index (Table 2 and Fig. 10c) and its combination with the *2320D* and the *2350D* indices helped to discriminate silicatic lithologies related to magmatic activity (i.e., Tertiary volcanics and the Precambrian Basement), enabling their masking before mapping the dolomite distribution (Figs. 10b and Figure 13a). In addition to these rocks, shown in red in Fig. 10c, it was noticed that the areas known from previous studies and fieldwork for the occurrence of hydrothermal dolomites are characterized by slightly lower *2200D* index values (shown in blue in Fig. 10c), if compared to other areas mapped as dolomite from the *2350D/2320D* ratio (Fig. 10b; green zones in Fig. 13a, b). Since higher *2200D* values are related to a higher relative abundance of Al-sheetsilicates, this feature could be due to the presence of micas and/or clays within the early diagenetic dolomite country rock (as also observed by Youssef (1998). Thus, the areas with dolomites (high *2320D/2350D*) and low *2200D* were interpreted as hydrothermal dolomites *sensu stricto*.

The main challenge in distinguishing between different dolomite types (i.e., hydrothermal and early diagenetic) is related to the relatively low spatial resolution of the space-borne hyperspectral instruments (i.e., ~30 m, as in the PRISMA specific case), as well as to the lack of characteristic spectral features achievable from SWIR spectra able to differentiate the dolomite facies in the studied wavelength region. For the Jabali case, the spatial resolution issue also affects the ability to differentiate the different carbonate units (Units 1 to 4), which are characterized by very small thicknesses (from 10 m to 40 m). Nevertheless, Kurz et al. (2012), who proposed a workflow combining ground-based hyperspectral imaging and lidar data for differentiating limestones from dolomites and characterizing also diagenetic and compositional features, achieved the results by using much higher spatial resolved hyperspectral data collected from a tripod-mounted sensor (HySpex SWIR-320 m imager). Lampinen et al. (2019), instead, evaluated the use of the Fe^{2+} CFA feature for discriminating between dolomite, siderite, and Fe-dolomite (+ankerite) from TIR trained SWIR drill core hyperspectral data. Good results were gained by applying the Fe^{2+} intensity scalar based on the measure of the depth of the Fe^{2+} reflectance absorption feature at ~ 1200 nm. A band ratio for Fe^{2+}-bearing minerals identification, including carbonates, and always based on the Fe^{2+} CFA feature, was proposed and successfully applied in previous studies to airborne hyperspectral data (Cudahy et al., 2008), e.g., the commercial HyMap system, equipped with a VNIR-SWIR spectrometer collecting 126 spectral bands at 3 to 10 m spatial resolution (depending on flying acquisition height). Potentially, a higher Fe^{2+} content in ore-related hydrothermal dolomites, compared to the one observed for the Jabali dolomites, could enable to use of the same bands for discriminating Fe-rich dolomites from Fe-poor dolomites even from satellite hyperspectral data, assisting the mineral identification and mapping even at the PRISMA spatial resolution, allowing the delineation of the ore-related alteration haloes from the barren diagenetic dolomite rocks.

6.2. *Delineation of gossans and mineralized outcrops*

The gossan samples analyzed in this study (Table 3, sampling areas 2, 3, 4, 5, 7 and Jabal Salab in Fig. 2) are dominated by goethite and hematite, displaying the main absorption features at 660 nm (CFT) and 908 nm to 910 nm (CFA) when goethite dominates, and the CFA shifted to shorter wavelengths (878 nm) when hematite occurs in higher amounts (e.g., sample JSMON18; Fig. 6). Moreover, the OH-related feature characteristic of a sufficient presence of jarosite,

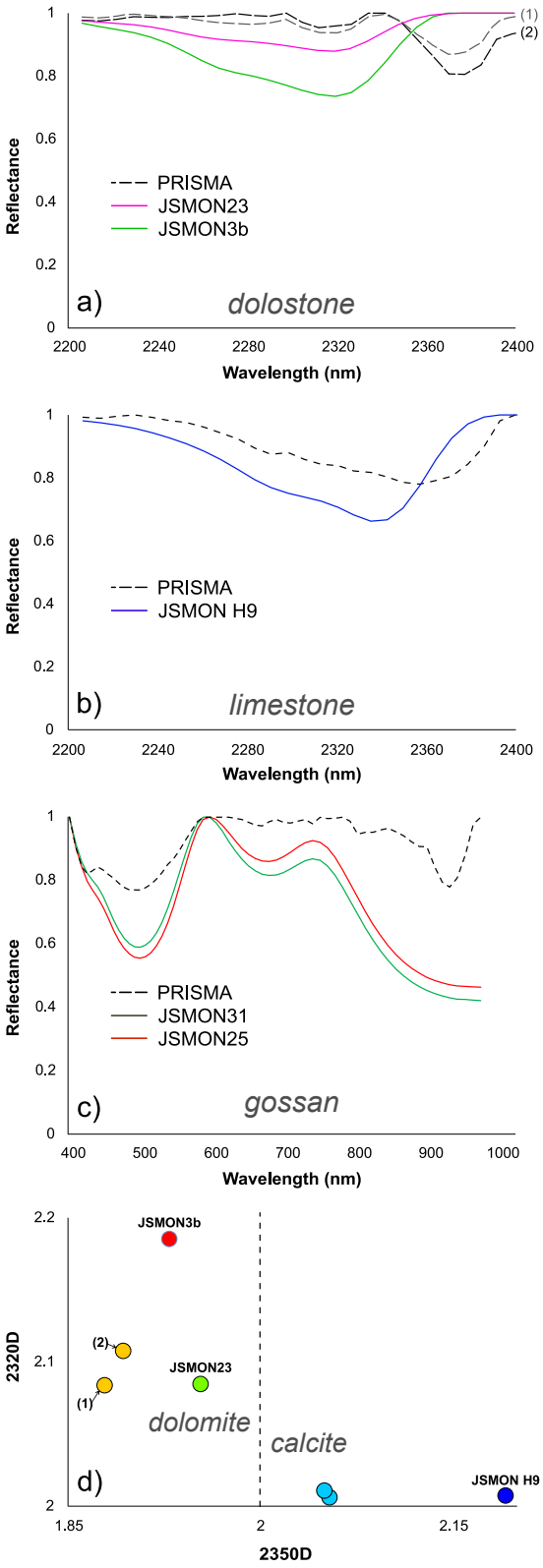

Fig. 12. Comparison between field-based representative spectra and PRISMA L2C. a) dolostones; b) limestones; c) gossans; d) 2350D versus 2320D validation binary plot, colored following the 2320D/2350D ratio. Only for field-based spectra, a label indicates the sample number. Dolomites (green to red dots) and limestones (light blue to dark blue dots) spectra are negatively correlated. (For interpretation of the references to color in this figure legend, the reader is referred to the web version of this article.)

plumbojarosite, and smectites is also visible in some samples (e.g., JSMON18; Fig. 6). The feature used for mineral mapping was the one at around 900 nm. As shown in Fig. 8d and 9d, it can discriminate all the gossan samples analyzed. The *900D* was applied to the whole samples hyperspectral dataset and plotted against the Hematite-Goethite ratio (Cudahy and Ramanaidou 1997) and the bulk Fe_2O_3 concentrations. It indicates that gossan samples are defined by higher *900D* values (Fig. 8d), and both goethite- and hematite-dominated samples display an increase of the *900D* values directly correlated with the goethite/hematite abundances obtained through XRPD-QPA analyses. A highly positive correlation is also shown in Fig. 9d, where higher Fe_2O_3 (wt%) bulk contents correspond to high *900D* values ($y = 96.756x - 196.58$, $R^2 = 0.93$). Fig. 11 a and b illustrate the application of the *900D* to the PRISMA L2C scene, after masking pixels with *2350D* < 2.0. In the resulting mineral distribution map (Fig. 11 a, and b), the known gossan outcrops are highlighted, but new gossans (i.e., new potential mineralized areas) were also identified (in yellow in Figure 13a and b), a few kilometers E-NE from the Jabali prospect area (Fig. 11b, Figure 13a and b).

With regards to the Zn-nonsulfides samples hyperspectral characterization, the smithsonite-hydrozincite bearing samples (JSMON29 and JSMAR8, Hyd > 20 wt%) are defined generally by broad absorption doublets at 2304 and 2400 nm (Fig. 7). Hemimorphite occurrence is, instead, commonly characterized by the Zn-OH bound displaying a very weak absorption at 2210 nm (JSMAR5, red spectrum in Fig. 7), however it occurs only in minor amounts in the studied samples. When either Fe-hydroxides (both goethite and amorphous phases) or Fe impurities are present, deep, and broad absorptions centered around 920 nm occur, summed to the contribution of Zn^{2+} in the same range. The overlapping of the CO_3^{2-} features of calcite, dolomite and Zn-bearing carbonate phases (i.e., smithsonite and hydrozincite) limits their clear distinction in the SWIR 2 region in any of the investigated samples (Fig. 7) due to mineral phases mixing. However, the ubiquitous presence of the broad absorption doublet when hydrozincite occurs in significant amounts in the mineral assemblage could be very useful for discriminating Zn-bearing nonsulfide phases from secondary calcite by employing portable hyperspectral instruments in the field.

An additional factor that can assist during the geo-mineralogical interpretation of hyperspectral maps is the possible association of hydrothermal-mineralized facies with tectonic structures (e.g., fractures and faults). In the Jabali case, for example, the hydrothermal alteration and the related mineralization at Jabali are preferentially located along faults and at their intersection following three main structural trends recognized in the field, associated with boundary faults at the flanks of basement highs (Figs. 1 and 2; Mondillo et al., 2014). Looking at Figure 13a and b, it is possible to see that the main targets in the Jabali area are defined by gossan occurrences in dolomites (identified through hyperspectral satellite imagery processing), and the position of main structural lineaments.

6.3. *PRISMA capabilities in mineral mapping*

The PRISMA surface reflectance data collected in the area appear to be suitable for mapping the target mineral phases in both the VNIR (around 900 nm) and SWIR 2 (between 2000 nm and 2400 nm) wavelength regions. In particular, the SWIR detector provides 171 spectral bands between 920 and 2500 nm, at an SNR ≥ 100 at wavelengths>2000 nm (Cogliati et al., 2021). Compared with previous studies based on remote sensing applications in the Jabali region (Deroin et al., 2011, 2012), where the use of Landsat (MSS, TM, ETM +), QuickBird, and ALOS AVNIR-2 multispectral satellite data led to a quite detailed mapping of the area, the narrower bands of the PRISMA SWIR 2 represent a more effective tool for discriminating SWIR-active spectrally similar minerals, like dolomite and calcite. Deroin et al. (2012, 2011) obtained a good identification of gossans possibly related to archeological remains, but carbonate species discrimination was only based on

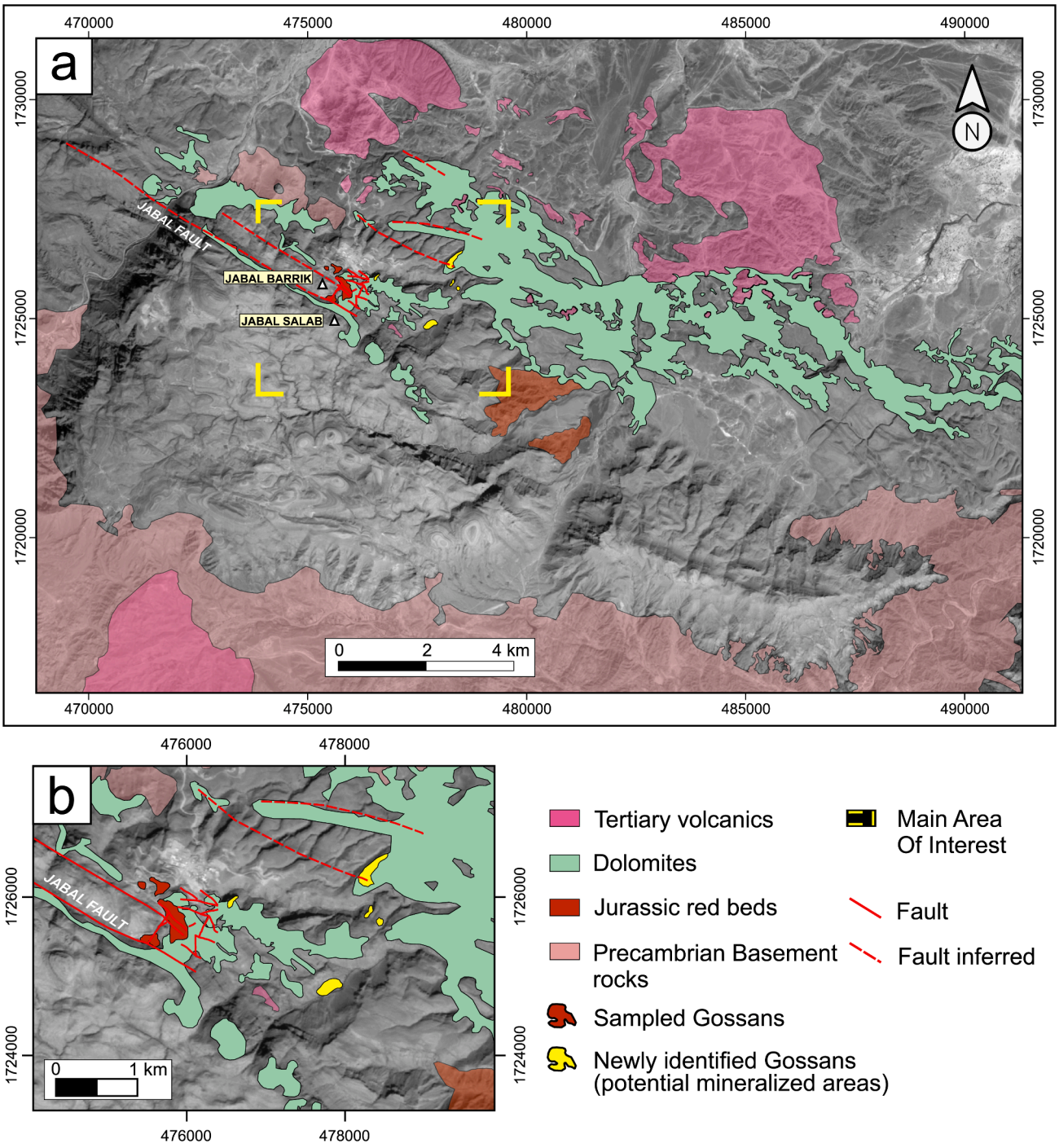

Fig. 13. (a) Geological interpretation resulting from the band depth indices and band ratio applied to the PRISMA L2C scene of the Jabali area and (b) a focus on the main area of interest. A subset of the PRISMA Panchromatic scene is used as background (pixel resolution 5 m).

the broad 30 m-SWIR 2 band 7 of Landsat (2.08–2.35 μm) and, therefore, it was less accurate due to poor coverage of the SWIR region. As shown in Fig. 12 a, b, and d, except for a slightly shift of the 2340–2342 nm calcite main feature (of ~ 7 nm), both dolomite and limestone are defined by the PRISMA spectra and are in agreement with the field-based hyperspectral data collected for validation and the geological features described in the area (Fig. 1b, 2). A shift of the calcite absorption feature was already encountered by (Heller Pearlshtien et al., 2021). However, (Heller Pearlshtien et al., 2021) observed a significant shift (29 nm versus ~ 7 nm observed in this study), resulting in inaccuracy in mapping. The authors explained the issue to be related to artefacts introduced for SWIR-2 long-wavelengths higher than 2340 nm by the L2D atmospheric correction process developed by ASI, and it was minimized by the same authors correcting radiance data instead of using L2D At-surface reflectance products. Therefore, even if the shift observed in this study is not so significant, and the limestone mapping, as well as its distinction from dolomites, could be performed by using the 2349 nm PRISMA band (B152 of the SWIR cube), the results can possibly even improve by using L1 data instead of applying the feature-based band ratios on already processed L2 images.

Due to the careful user-guided evaluation of the PRISMA bands before proceeding with the mineral mapping, the PRISMA-derived spectral maps appeared only slightly influenced by the striping effect, which represented the main issue for some specific and diagnostic

absorption bands and regions in mineral mapping. Generally, they are noticeable in the form of noisy bands with along-track lines with no spectral information, and other noise distortions that, for the PRISMA scene from the Jabali area, are characterized by some of the bands used for the *2320D* and the *900D* indices. The accuracy in the detection of the geological features of the area was only negligibly impacted, since it is covered with hardly any green and dry vegetation which may contribute to mixing effects (Cudahy et al., 2008).

7. Conclusions

The results of this study illustrate the advantages of using feature extraction indices applied to hyperspectral data for recognition of outcropping geology, that can be used as a powerful tool for mineral exploration in sedimentary environments at regional scale. Since the understanding of the mineralogical and geochemical features in both country rocks and weathering profiles is crucial for enabling successful exploration, we adopted a combined use of remote and proximal sources of hyperspectral data for defining features possibly able to target carbonate-hosted Zn-Pb ore deposits. The VNIR-SWIR reflectance spectroscopic data derived from the PRISMA satellite, that were interpreted with the support of analyses on ground samples, allowed us to (1) delineate the distribution of the dolomitization in the Jabali area, enabling its discrimination from limestones, and (2) identify the gossan outcrops overlying the mineralized areas. The detailed evaluation of the reflectance spectra from mineralized samples, even if their distribution mapping is not achievable at the satellite spatial resolution, helped the definition of the spectral responses of Zn(-Pb)-bearing oxidation-related minerals. Since they are commonly associated with nonsulfide ores related to supergene alteration of sulfide ore bodies, they represent a useful tool for exploration surveys based on field spectroscopy.

In conclusion, this study demonstrates that PRISMA can be a valuable tool for mineral exploration. The proposed method could be potentially applied to other hydrothermal ore deposits in sedimentary environments, including sedimentary-exhalative (SEDEX) Pb-Zn ores, hypogene willemite nonsulfide deposits (e.g., Vazante district, Beltana, and Berg Aukas deposits; Hitzman et al., 2003), as well as many hydrocarbon reservoirs (Davies and Smith 2006). Each of the latter systems displays a strong structural control by extensional and/or strike-slip (wrench) faults, typically acting as preferential paths for fluid flow and controlling the hydrothermal alteration of country rocks. An extension to other spectral ranges (e.g., Thermal InfraRed – TIR) can also be considered, applying the method proposed to other case studies and systems defined by VNIR-SWIR non-active alteration minerals and lithologies. Distinguishing diverse dolomite types (i.e., hydrothermal vs early diagenetic) has not been solved in the current study using PRISMA, mostly due to limitations in the satellite spatial resolution. More investigation is necessary to develop and improve methods for noise suppression (e.g., de-striping) for some wavelength regions of the PRISMA data.

8. Data access

Project carried out using PRISMA Products, © of the Italian Space Agency (ASI), delivered under an ASI License to use by visiting prisma.asi.it.

CRediT authorship contribution statement

Rita Chirico: Conceptualization, Formal analysis, Data curation, Software, Visualization, Validation, Writing – original draft. **Nicola Mondillo:** Conceptualization, Supervision, Funding acquisition, Project administration, Writing – review & editing. **Carsten Laukamp:** Methodology, Supervision, Investigation, Writing – review & editing. **Angela Mormone:** Data curation. **Diego Di Martire:** Writing – review & editing. **Alessandro Novellino:** Supervision. **Giuseppina Balassone:** Writing – review & editing.

Declaration of Competing Interest

The authors declare that they have no known competing financial interests or personal relationships that could have appeared to influence the work reported in this paper.

Data availability

Data will be made available on request.

Acknowledgments

This work was supported by the Ph.D. scholarship Complementary Operational Program (POC) “Research and Innovation 2014–2020”, co-financed by the Italian Ministry of University and Research and European Social Fund (ESF) 2014–2020, Project Supervisor: Nicola Mondillo. Scientific partners of the Project: CSIRO Mineral Resources and the British Geological Survey (BGS).

R. Chirico and coauthors would like to thank the Italian Space Agency (ASI) for having funded the PRISMA mission and for releasing free-of-charge hyperspectral images to the scientific community. The authors would like to thank the entire Mineral Resources team at CSIRO for their support.

References

Agenzia Spaziale Italiana (ASI) (2020) PRISMA Products Specification Document Issue 2.1 Date 12/02/2020.

Al Ganad, I., Lagny, P., Lescuyer, J.L., Ramboz, C., Touray, J.C., 1994. Jabali, a Zn-Pb-(Ag) carbonate-hosted deposit associated with Late Jurassic rifting in Yemen. Miner. Depos. 29 (1), 44–56.

Amato, U., Antoniadis, A., Carfora, M.F., Colandrea, P., Cuomo, V., Franzese, M., Pignatti, S., Serio, C., 2013. Statistical classification for assessing PRISMA hyperspectral potential for agricultural land use. IEEE J. Sel. Top. Appl. Earth Obs. Remote Sens. 6 (2), 615–625.

As-Saruri, M.A., Sorkhabi, R., Baraba, R., 2010. Sedimentary basins of Yemen: their tectonic development and lithostratigraphic cover. Arab. J. Geosci. 3 (4), 515–527.

Bedini, E., 2017. The use of hyperspectral remote sensing for mineral exploration: a review. J. Hypersp. Remote Sens. 7, 189–211. https://doi.org/10.29150/jhrs.v7.4.p189-211.

Bedini, E., Chen, J., 2020. Application of PRISMA satellite hyperspectral imagery to mineral alteration mapping at Cuprite, Nevada, USA. J. Hyperspec. Remote Sens. 10, 87–94.

Bish, D.L., Post, J.E., 1993. Quantitative mineralogical analysis using the Rietveld full-pattern fitting method. Am. Mineral. 78, 932–940.

Bishop, J.L., Murad, E., 2005. The visible and infrared spectral properties of jarosite and alunite. Am. Mineral. 90, 1100–1107. https://doi.org/10.2138/am.2005.1700.

Boni, M., Mondillo, N., Balassone, G., 2011. Zincian dolomite: a peculiar dedolomitization case? Geology 39, 183–186. https://doi.org/10.1130/G31486.1.

Casa R, Pignatti S, Pascucci S, et al (2020) Assessment of PRISMA imaging spectrometer data for the estimation of topsoil properties of agronomic interest at the field scale. 6728. https://doi.org/10.5194/egusphere-egu2020-6728.

Christmann P, Lagny P, Lescuyer J-L, Sharaf Ad Din A (1989) Discovery of the Jabali deposit (Zn-Pb-Ag) in the Jurassic cover of the Yemen Arab Republic. Chronique de la recherche minière 43–52.

Chung, F.H., 1974a. Quantitative interpretation of X-ray diffraction patterns of mixtures. I. Matrix-flushing method for quantitative multicomponent analysis. J. Appl. Cryst. 7, 519–525. https://doi.org/10.1107/S0021889874010375.

Chung, F.H., 1974b. Quantitative interpretation of X-ray diffraction patterns of mixtures. II. Adiabatic principle of X-ray diffraction analysis of mixtures. J Appl Cryst 7, 526–531. https://doi.org/10.1107/S0021889874010387.

Clark, R.N., King, T.V.V., Klejwa, M., Swayze, G.A., Vergo, N., 1990. High spectral resolution reflectance spectroscopy of minerals. J. Geophys. Res. Solid Earth 95 (B8), 12653.

Cogliati, S., Sarti, F., Chiarantini, L., Cosi, M., Lorusso, R., Lopinto, E., Miglietta, F., Genesio, L., Guanter, L., Damm, A., Pérez-López, S., Scheffler, D., Tagliabue, G., Panigada, C., Rascher, U., Dowling, T.P.F., Giardino, C., Colombo, R., 2021. The PRISMA imaging spectroscopy mission: overview and first performance analysis. Remote Sens. Environ. 262 https://doi.org/10.1016/j.rse.2021.112499.

Crowley, J.K., 1986. Visible and near-infrared spectra of carbonate rocks: Reflectance variations related to petrographic texture and impurities. J. Geophys. Res. Solid Earth 91, 5001–5012. https://doi.org/10.1029/JB091iB05p05001.

Crowley, J.K., 1991. Visible and near-infrared (0.4–2.5 μm) reflectance spectra of Playa evaporite minerals. J. Geophys. Res. Solid Earth 96, 16231–16240. https://doi.org/10.1029/91JB01714.

Crowley, J.K., Brickey, D.W., Rowan, L.C., 1989. Airborne imaging spectrometer data of the Ruby Mountains, Montana: Mineral discrimination using relative absorption band-depth images. Remote Sens. Environ. 29, 121–134. https://doi.org/10.1016/0034-4257(89)90021-7.

Crowley, J.K., Williams, D.E., Hammarstrom, J.M., et al., 2003. Spectral reflectance properties (0.4–2.5 μm) of secondary Fe-oxide, Fe-hydroxide, and Fe-sulphate-hydrate minerals associated with sulphide-bearing mine wastes. Geochemi. Explor. Environ. Anal. 3, 219–228. https://doi.org/10.1144/1467-7873/03-001.

Cudahy, T., Jones, M., Thomas, M., Laukamp, C., Caccetta, M., Hewson, R., Rodger, A., Verrall, M., 2008. Next Generation Mineral Mapping: Queensland airborne HyMap and satellite ASTER surveys 2006–2008.

Cudahy, T., Ramanaidou, E.R., 1997. Measurement of the hematite:goethite ratio using field visible and near-infrared reflectance spectrometry in channel iron deposits, Western Australia. Aust. J. Earth Sci. 44, 411–420. https://doi.org/10.1080/08120099708728322.

Curtiss, B., 1985. Evaluation of the Physical Properties of Naturally Occurring Iron (III) Oxyhydroxides on Rock Surfaces in Arid and Semi-arid Regions Using Visible and Near Infrared Reflectance Spectroscopy.

Davies, G.R., Smith Jr, L.B., 2006. Structurally controlled hydrothermal dolomite reservoir facies: an overview. AAPG Bull. 90, 1641–1690. https://doi.org/10.1306/05220605164.

De Bonis R, Laneve G, Palombo A, et al (2015) The potential impact of the next hyperspectral prisma mission on the natural and anthropogenic hazards management. In: 2015 IEEE 15th International Conference on Environment and Electrical Engineering (EEEIC). pp 1643–1646.

Deroin, J.-P., Téreygeol, F., Heckes, J., 2011. Evaluation of very high to medium resolution multispectral satellite imagery for geoarchaeology in arid regions – Case study from Jabali, Yemen. J. Archaeol. Sci. 38, 101–114. https://doi.org/10.1016/j.jas.2010.08.015.

Deroin, J.-P., Téreygeol, F., Heckes, J., 2012. Remote Sensing Study of the Ancient Jabali Silver Mines (Yemen): From Past to Present. In: Lasaponara, R., Masini, N. (Eds.), SAtellite Remote Sensing: A New Tool for ArchAeology. Springer, Netherlands, Dordrecht, pp. 231–245.

European Space Agency, 2015. Sentinel-2 User Handbook. ESA Standard Document Date 1, 1–64.

Farr, T.G., Rosen, P.A., Caro, E., Crippen, R., Duren, R., Hensley, S., Kobrick, M., Paller, M., Rodriguez, E., Roth, L., Seal, D., Shaffer, S., Shimada, J., Umland, J., Werner, M., Oskin, M., Burbank, D., Alsdorf, D., 2007. The Shuttle radar topography mission. Rev. Geophys. 45 (2) https://doi.org/10.1029/2005RG000183.

Gaffey, S.J., 1985. Reflectance spectroscopy in the visible and near-infrared (0.35–2.55 μm): applications in carbonate petrology. Geology 13, 270–273. https://doi.org/10.1130/0091-7613(1985)13<270:RSITVA>2.0.CO;2.

Gaffey, S.J., 1986. Spectral reflectance of carbonate minerals in the visible and near infrared (0.35-2.55 microns); calcite, aragonite, and dolomite. Am. Mineral. 71, 151–162.

Giardino, C., Bresciani, M., Braga, F., Fabbretto, A., Ghirardi, N., Pepe, M., Gianinetto, M., Colombo, R., Cogliati, S., Ghebrehiwot, S., Laanen, M., Peters, S., Schroeder, T., Concha, J.A., Brando, V.E., 2020. First Evaluation of PRISMA Level 1 data for water applications. Sensors 20 (16), 4553.

Green, D., Schodlok, M., 2016. Characterisation of carbonate minerals from hyperspectral TIR scanning using features at 14 000 and 11 300 nm. Aust. J. Earth Sci. 63, 951–957. https://doi.org/10.1080/08120099.2016.1225601.

Gualtieri, A.F., 2000. Accuracy of XRPD QPA using the combined Rietveld–RIR method. J Appl Cryst 33, 267–278. https://doi.org/10.1107/S002188989901643X.

Gualtieri, A., Norby, P., Hanson, J., Hriljac, J., 1996. Rietveld refinement using synchrotron X-ray powder diffraction data collected in transmission geometry using an imaging-plate detector: application to standard m-ZrO2. J Appl Cryst 29, 707–713. https://doi.org/10.1107/S0021889896008199.

Guanter, L., Irakulis-Loitxate, I., Gorroño, J., Sánchez-García, E., Cusworth, D.H., Varon, D.J., Cogliati, S., Colombo, R., 2021. Mapping methane point emissions with the PRISMA spaceborne imaging spectrometer. Remote Sens. Environ. 265 https://doi.org/10.1016/j.rse.2021.112671.

Haest, M., Cudahy, T., Laukamp, C., Gregory, S., 2012a. Quantitative Mineralogy from Infrared Spectroscopic Data. I. Validation of mineral abundance and composition scripts at the rocklea channel iron deposit in Western Australia. Econ. Geol. 107, 209–228. https://doi.org/10.2113/econgeo.107.2.209.

Haest, M., Cudahy, T., Laukamp, C., Gregory, S., 2012b. Quantitative mineralogy from infrared spectroscopic data. II. Three-dimensional mineralogical characterization of the rocklea channel iron deposit, Western Australia. Econ. Geol. 107, 229–249. https://doi.org/10.2113/econgeo.107.2.229.

Heller Pearlshtien, D., Pignatti, S., Greisman-Ran, U., Ben-Dor, E., 2021. PRISMA sensor evaluation: a case study of mineral mapping performance over Makhtesh Ramon, Israel. Int. J. Remote Sens. 42, 5882–5914. https://doi.org/10.1080/01431161.2021.1931541.

Hitzman, M.W., Reynolds, N.A., Sangster, D.F., Allen, C.R., Carman, C.E., 2003. Classification, genesis, and exploration guides for nonsulfide zinc deposits. Econ. Geol. 98 (4), 685–714.

Hunt, G.R., 1971. Visible and near-infrared spectra of minerals and rocks: III. Oxides and hydro-oxides. Modern Geology 2, 195–205.

Hunt, G.R., 1977. Spectral signatures of particulate minerals in the visible and near infrared. Geophysics 42, 501–513. https://doi.org/10.1190/1.1440721.

Hunt, G.R., Ashley, R.P., 1979. Spectra of altered rocks in the visible and near infrared. Econ. Geol. 74, 1613–1629. https://doi.org/10.2113/gsecongeo.74.7.1613.

Hunt, G.R., Salisbury, J.W., 1971. Visible and near infrared spectra of minerals and rocks II. Carbonates. Modern Geol. 2, 23–30.

Kale, K.V., Solankar, M.M., Nalawade, D.B., Dhumal, R.K., Gite, H.R., 2017. A research review on hyperspectral data processing and analysis algorithms. Proc Natl Acad Sci, India, Sect A Phys Sci 87 (4), 541–555.

Kurz, T.H., Dewit, JULIE, Buckley, S.J., Thurmond, J.B., Hunt, D.W., Swennen, RUDY, 2012. Hyperspectral image analysis of different carbonate lithologies (limestone, karst and hydrothermal dolomites): the Pozalagua Quarry case study (Cantabria, North-west Spain). Sedimentology 59 (2), 623–645.

Lampinen, H.M., Laukamp, C., Occhipinti, S.A., Metelka, V., Spinks, S.C., 2017. Delineating alteration footprints from field and ASTER SWIR spectra, geochemistry, and gamma-ray spectrometry above Regolith-covered base metal deposits—An example from abra, Western Australia. Econ. Geol. 112 (8), 1977–2003.

Lampinen, H.M., Laukamp, C., Occhipinti, S.A., Hardy, L., 2019. Mineral footprints of the paleoproterozoic sediment-hosted abra pb-Zn-Cu-Au deposit Capricorn Orogen, Western Australia. Ore Geol. Rev. 104, 436–461. https://doi.org/10.1016/j.oregeorev.2018.11.004.

Laukamp, C., Cudahy, T., Thomas, M., Jones, M., Cleverley, J.S., Oliver, N.H.S., 2011. Hydrothermal mineral alteration patterns in the Mount Isa Inlier revealed by airborne hyperspectral data. Aust. J. Earth Sci. 58 (8), 917–936.

Laukamp, C., Termin, K.A., Pejcic, B., Haest, M., Cudahy, T., 2012. Vibrational spectroscopy of calcic amphiboles – applications for exploration and mining. Eur. J. Mineral. 24 (5), 863–878.

Laukamp, C., Rodger, A., LeGras, M., Lampinen, H., Lau, I.C., Pejcic, B., Stromberg, J., Francis, N., Ramanaidou, E., 2021. Mineral physicochemistry underlying feature-based extraction of mineral abundance and composition from shortwave, mid and thermal infrared reflectance spectra. Minerals 11 (4), 347.

Laukamp, C., LeGras, M., Montenegro, V., Windle, S., McFarlane, A., 2022. Grandite-based resource characterization of the skarn-hosted Cu-Zn-Mo deposit of Antamina, Peru. Miner Depos. 57 (1), 107–128.

Laukamp, C., 2022. Geological Mapping using mineral absorption feature-guided band-ratios applied to PRISMA satellite hyperspectral level 2D imagery IGARSS 2022 2022 Kuala Lumpur, Malaysia 17.-22.07.22.

Leach DL, Sangster DF, Kelley KD, et al (2005). Sediment-Hosted Lead-Zinc Deposits: A Global Perspective, in: Hedenquist, J.W., Thompson, J.F.H., Goldfarb, R.J., Richards, J.P. (Eds.), One Hundredth Anniversary Volume. Society of Economic Geologists, p. 0. https://doi.org/10.5382/AV100.18.

Loizzo R, Guarini R, Longo F, et al (2018) Prisma: The Italian Hyperspectral Mission. In: IGARSS 2018 - 2018 IEEE International Geoscience and Remote Sensing Symposium. pp 175–178.

Malvern Panalytical. https://www.malvernpanalytical.com/ (accessed 26 May 2022).

McCombe, D., Fernette, G., Aalawi, A., 1994. The geological and mineral resources of Yemenf Ministry of oil and Mineral Resources, Geological Survey of Yemen 1994 Sana'a. Yemen.

McConachy, T.F., Yang, K., Boni, M., Evans, N.J., 2007. Spectral reflectance: preliminary data on a new technique with potential for non-sulphide base metal exploration. Geochem. Explor. Environ, Anal. 7, 139–151. https://doi.org/10.1144/1467-7873/07-129.

Mondillo, N., Boni, M., Balassone, G., Grist, B., 2011. In search of the lost zinc: a lesson from the Jabali (Yemen) nonsulfide zinc deposit. J. Geochem. Explor. 108, 209–219. https://doi.org/10.1016/j.gexplo.2011.02.010.

Mondillo, N., Boni, M., Balassone, G., Joachimski, M., Mormone, A., 2014. The Jabali nonsulfide Zn–Pb–Ag deposit, western Yemen. Ore Geol. Rev. 61, 248–267.

NASA JPL (2013) NASA Shuttle Radar Topography Mission Global 1 arc second.

Niroumand-Jadidi, M., Bovolo, F., Bruzzone, L., 2020. Water quality retrieval from PRISMA hyperspectral images: first experience in a Turbid Lake and comparison with sentinel-2. Remote Sens. (Basel) 12, 3984. https://doi.org/10.3390/rs12233984.

Ostendorf, J., Henjes-Kunst, F., Mondillo, N., et al., 2015. Formation of Mississippi Valley–type deposits linked to hydrocarbon generation in extensional tectonic settings: Evidence from the Jabali Zn-Pb-(Ag) deposit (Yemen). Geology 43, 1055–1058. https://doi.org/10.1130/G37112.1.

Pepe, M., Pompilio, L., Gioli, B., Busetto, L., Boschetti, M., 2020. Detection and classification of non-photosynthetic vegetation from PRISMA hyperspectral data in croplands. Remote Sens. (Basel) 12 (23), 3903.

Peyghambari, S., Zhang, Y., 2021. Hyperspectral remote sensing in lithological mapping, mineral exploration, and environmental geology: an updated review. JARS 15, 031501. https://doi.org/10.1117/1.JRS.15.031501.

Pignatti, S., Palombo, A., Pascucci, S., et al., 2013. The PRISMA hyperspectral mission: Science activities and opportunities for agriculture and land monitoring. In: In: 2013 IEEE International Geoscience and Remote Sensing Symposium - IGARSS, pp. 4558–4561.

Romaniello, V., Spinetti, C., Silvestri, M., Buongiorno, M.F., 2021. A Methodology for CO2 retrieval applied to hyperspectral PRISMA data. Remote Sens. (Basel) 13, 4502. https://doi.org/10.3390/rs13224502.

Romaniello, V., Buongiorno, M.F., Spinetti, C., Silvestri, M., 2022. Analysis of volcanic carbon dioxide emissions by means of prisma hyperspectral data and in situ measurements. In: In: IGARSS 2022–2022 IEEE International Geoscience and Remote Sensing Symposium, pp. 7268–7271.

Santoro, L., Putzolu, F., Mondillo, N., Herrington, R., Najorka, J., Boni, M., Balassone, G., 2021. Quantitative mineralogical evaluation of Ni-Co laterite ores through XRPD-QPA-and automated SEM-based approaches: The Wingellina (Western Australia) case study. J. Geochem. Explor. 223, 106695.

Santoro, L., Rollinson, G.K., Boni, M., Mondillo, N., 2015. Automated scanning electron microscopy (QEMSCAN®)-based mineral identification and quantification of the Jabali Zn-Pb-Ag nonsulfide deposit (Yemen). Econ. Geol. 110, 1083–1099. https://doi.org/10.2113/econgeo.110.4.1083.

Savitzky, A., Golay, M.J., 1964. Smoothing and differentiation of data by simplified least squares procedures. Anal. Chem. 36 (8), 1627–1639.
Scheinost, A.C., Schulze, D.G., Schwertmann, U., 1999. Diffuse reflectance spectra of A1 substituted goethite: a ligand field approach. Clay Clay Miner. 47, 156–164.
Sonntag, I., Laukamp, C., Hagemann, S.G., 2012. Low potassium hydrothermal alteration in low sulfidation epithermal systems as detected by IRS and XRD: An example from the Co–O mine, Eastern Mindanao, Philippines. Ore Geol. Rev. 45, 47–60. https://doi.org/10.1016/j.oregeorev.2011.08.001.
SRK Consulting, 2005. Jabali feasibility study, geology and resources. Unpublished report, ZincOx Resources plc., p. 45.
Taylor, R. (Ed.), 2011. Gossans and Leached Cappings. Springer Berlin Heidelberg, Berlin, Heidelberg.
The Spectral Geologist (TSG™) https://research.csiro.au/thespectralgeologist (accessed 25 November 2021).
Van der Meer, F.D., 1995. Spectral reflectance of carbonate mineral mixtures and bidirectional reflectance theory: Quantitative analysis techniques for application in remote sensing. Remote Sens. Rev. 13, 67–94. https://doi.org/10.1080/02757259509532297.
Van der Meer, F.D., 2004. Analysis of spectral absorption features in hyperspectral imagery. Int. J. Appl. Earth Obs. 5, 55–68. https://doi.org/10.1016/j.jag.2003.09.001.
Van der Meer, F.D., van der Werff, H.M.A., van Ruitenbeek, F.J.A., Hecker, C.A., Bakker, W.H., Noomen, M.F., van der Meijde, M., Carranza, E.J.M., Smeth, J.B.d., Woldai, T., 2012. Multi- and hyperspectral geologic remote sensing: a review. Int. J. Appl. Earth Obs. Geoinf. 14 (1), 112–128.
Vangi, E., D'Amico, G., Francini, S., Giannetti, F., Lasserre, B., Marchetti, M., Chirici, G., 2021. The new hyperspectral satellite PRISMA: imagery for forest types discrimination. Sensors 21 (4), 1182.
Vedder, W., 1964. Correlations between infrared spectrum and chemical composition of mica. Am. Mineral. 49, 736–768.
Vedder, W., McDonald, R.S., 1963. Vibrations of the OH Ions in Muscovite. J Chem Phys 38, 1583–1590. https://doi.org/10.1063/1.1776925.
Windeler, D.S., Lyon, R.J., 1991. Discriminating dolomitization of marble in the Ludwig Skarn near Yerington, Nevada using high-resolution airborne infrared imagery. Photogramm Eng Remote Sensing 57 (9), 1171–1177.
Youssef, E.S.A.A., 1998. Sequence stratigraphy of the upper jurassic evaporite-carbonate: sequence at the western area of Wadi Al-Jawf-Marib basin, Yemen. Carbonates Evaporites 13, 168–173. https://doi.org/10.1007/BF03176590.
Zaini, N., Van der Meer, F., Van der Werff, H., 2012. Effect of grain size and mineral mixing on carbonate absorption features in the SWIR and TIR wavelength regions. Remote Sens. 4 (4), 987–1003.